

Epidemic models characterize seizure propagation and the effects of epilepsy surgery in individualized brain networks based on MEG and invasive EEG recordings

Ana. P. Millán^{1,*}, Elisabeth C.W. van Straaten¹, Cornelis J. Stam¹, Ida A. Nissen¹, Sander Idema², Johannes C. Baayen², Piet Van Mieghem³, and Arjan Hillebrand¹

¹Department of Clinical Neurophysiology and MEG Center, Amsterdam Neuroscience, Vrije Universiteit Amsterdam, Amsterdam UMC, Amsterdam, The Netherlands

²Department of Neurosurgery, Amsterdam Neuroscience, Vrije Universiteit Amsterdam, Amsterdam UMC, Amsterdam, The Netherlands

³Faculty of Electrical Engineering, Mathematics and Computer Science, Delft University of Technology, Delft, The Netherlands

*Corresponding author: a.p.millanvidal@amsterdamumc.nl

Abstract

Background

Epilepsy surgery is the treatment of choice for drug-resistant epilepsy patients. However, seizure-freedom is currently achieved in only 2/3 of the patients after surgery. In this study we have developed an individualized computational model based on [MEG brain networks](#) to explore seizure propagation and the efficacy of different virtual resections. Eventually, the goal is to obtain individualized models to optimize resection strategy and outcome.

Methods

We have modelled seizure propagation as an epidemic process using the susceptible-infected (SI) model on individual [brain networks](#) derived from presurgical MEG. We included 10 patients who had received epilepsy surgery and for whom the surgery outcome at least one year after surgery was known. The model parameters were tuned in order to reproduce the patient-specific seizure propagation patterns as recorded with invasive EEG. We defined a personalized search algorithm that combined structural and dynamical information to find resections that maximally decreased seizure propagation for a given resection size. The optimal resection for each patient was defined as the smallest resection leading to at least a 90% reduction in seizure propagation.

Results

The individualized model reproduced the basic aspects of seizure propagation for 9 out of 10 patients when using the resection area as the origin of epidemic spreading, and for 10 out of 10 patients with an alternative definition of the seed region. We found that, for 7 patients, the optimal resection was smaller than the resection area, and for 4 patients we also found that a resection smaller than the resection area could lead to a 100% decrease in propagation. Moreover, for two cases these alternative resections included nodes outside the resection area.

Conclusion

Epidemic spreading models fitted with patient specific data can capture the fundamental aspects of clinically observed seizure propagation, and can be used to test virtual resections *in silico*. Combined with optimization algorithms, smaller or alternative resection strategies, that are individually targeted for each patient, can be determined with the ultimate goal to improve surgery outcome. [MEG-based networks can provide a good approximation of structural connectivity for seizure spreading computational models, and facilitate their clinical use.](#)

1 Introduction

Epilepsy is one of the most common neurological disorders, affecting between 4 and 10 per 1000 people worldwide [1]. There is not one single cause of epilepsy: it often occurs as an associated symptom of an underlying disease, but many other times it is produced by unknown causes [2]. This complicates the understanding of seizure dynamics, and to this day the microscopic mechanisms that lead to seizure generation and propagation are not fully understood [3]. It is generally assumed that a shift from normal neuronal activity to excessive synchronization [4] occurs due to decreased inhibition [5], but the actual nature of this transition is not clear.

Epilepsy is initially treated by anti-epileptic drugs (AEDs), but this approach is not effective for roughly 1 out of 3 people [6]. For these drug-resistant patients, epilepsy surgery is an optional treatment if a focal origin of the seizures can be found. The surgery then aims to remove or disconnect the brain regions thought to be involved in seizure generation. Currently, seizure freedom is achieved in up to 2 out of 3 patients who undergo epilepsy surgery, although surgery outcome varies greatly depending on epilepsy type [7]. Even when surgery is not completely successful, the majority of patients will still experience a reduction in seizure frequency or intensity after surgery. However, side-effects and cognitive complaints can also occur after surgery. These depend on the brain areas resected, but are difficult to predict accurately [8].

Traditionally, efforts to improve epilepsy surgery have aimed to better characterize the epileptogenic zone (EZ, defined as the minimal brain area or areas that need to be removed or disconnected to achieve seizure freedom [9]; by definition, this can only be confirmed after surgery, and prior to it only a hypothesis can be made). However, in recent years – and in line with the increasingly common view of the brain as a complex network – epilepsy is seen as a network disorder. Attention is thus shifting towards the definition of *epileptogenic networks* that can capture more details of seizure dynamics and the distribution of epileptiform activity [10–12]. An increasing number of findings support this perspective: topological properties of epileptogenic brain networks have been found to deviate from those seen in healthy controls [13, 14], and abnormal patterns of functional connectivity emerge [15–17] (although the results of different imaging modalities are sometimes contradictory [15–20]). A common finding in pathological brain networks is the association of disease with network hubs [21, 22]. In the case of epilepsy, hubs may facilitate the propagation of epileptiform activity to the rest of the brain [23–25]. Moreover, several studies have pointed out the existence of *pathological hubs*: abnormal, hyperconnected regions in the vicinity of the epileptic focus, which may facilitate seizure propagation [25–27].

Importantly, the network perspective of epilepsy implies that the effect of a resection cannot be predicted directly from the location of the removed region alone [28]: local resections can have widespread effects, but at the same time might not prevent the epileptogenic network from forming a new EZ eventually [29]. Computer models are then necessary to help predict the effect of a given resection [30]. Integrating patient specific data of different modalities, computer models allow us to test different resections *in silico* – i.e. using virtual resections – together with different markers of the EZ. Within this framework, Hebbink et al. [31] showed that the resection of the pathological network node is not necessarily the best approach to alleviate seizures, whereas Lopes et al. [32] found that the fraction of resected rich-club nodes correlated with surgery outcome. Going beyond topological network analysis, the simulation of ictal activity on top of brain networks can aid the identification of the EZ and prediction of surgery outcome, as well as predict possible side-effects. Such computational models can be used to identify epileptogenic areas [33, 34] or analyze different resection strategies [26, 32, 35–38], such that patient-specific resection strategies, that may lead to a better outcome or fewer side-effects than the standard surgery, can be tested [33, 39–41]. Validation of the models is usually attempted by looking for differences in the model predictions between seizure free and non-seizure free patients [42, 43] or by correlating seizure propagation on the model with the empirical data [44].

A basic consideration in the model definition is thus the nature of the underlying network. The temporal and spatial resolution of the resulting network-based model, and the interpretation of the connections between regions, will depend on the modality that was used to define the network structure. Studies on epileptogenic networks have considered both functional [32, 35, 37, 42, 43, 45] and structural [33, 36, 40, 41] networks, as they are both affected in patients with epilepsy [40–43]. However, functional networks can capture abnormalities in brain activity even in the absence of structural abnormalities [46]. Functional networks based on intracranial recordings [32, 35, 37, 42, 43] usually include ictal data and allow for highly precise characterization of some brain areas, however spatial sampling is sparse and biased due to an a priori hypothesis of the EZ, which may lead to bias in the analysis. Moreover, these invasive recordings are not always part of the presurgical evaluation. Non-invasive methods, such as Electro- and Magneto-Encephalography (EEG/MEG) have no risks of complications [47]. MEG is less affected by the skull and other tissue in the head, is reference-free and has higher spatial resolution than clinical scalp EEG [48]. This allows for a more accurate estimation of functional interactions between brain regions, and thus a more accurate reconstruction of the functional networks. MEG interictal resting-state functional brain networks have been used previously to identify the EZ [11, 27].

99 In general, most of the studies cited above made use of highly detailed non-linear models, such as neural mass
100 models or theta models [49]. These models depend on several parameters that need to be adjusted beforehand,
101 which complicates the optimization of the model and makes it difficult to obtain conclusions that are gener-
102 alizable. As it is usually the case, an interplay exists between the generalizability and accuracy of the model,
103 such that optimizing the predictive power of a model often means reducing the number of tunable parameters
104 [50]. Thus, simpler models with few parameters might prove more reproducible, especially if the behavior of
105 the model is understood mathematically. In this regard, one particular framework of relative mathematical
106 simplicity that may capture the fundamental aspects of seizure propagation is that of epidemic spreading models
107 [51]. These models simulate the propagation of an agent from some given location to other connected areas, a
108 basic phenomenon appearing in a multitude of systems. Such models have been used, for instance, to study the
109 spreading of pathological proteins on brain networks [52], or the relation between brain structure and function
110 [53].

111 We propose that epidemic models can also provide a good representation of the initial steps of seizure
112 propagation, during which the anomalous highly synchronized ictal activity propagates from the EZ to other
113 regions. Moreover, as it is the case in epilepsy surgery, studies on epidemic models often try to find ways to
114 stop or limit the propagation of the epidemics. Thus, epidemic models could also aid the planning of epilepsy
115 surgery. For instance, the fundamental role of hubs in propagation is a well-known result of epidemic spreading
116 [54], and targeting hub regions is often the most efficient way to obtain global immunization [55, 56]. Data of
117 outbreak patterns can also be used retroactively to find the location of the origin of an epidemic [57, 58]. Within
118 this framework, in a previous study [41] we modelled seizure propagation as an epidemic spreading process and,
119 using the eigenvector centrality as a surrogate measure, found that the size of the resection area could be largely
120 reduced with only a small decrease in the efficacy of the virtual surgery.

121 Here we defined an individualized seizure propagation model by making use of the Susceptible-Infectious (SI)
122 model of epidemic spreading on top of a global brain network, for a group of 10 epilepsy patients who underwent
123 epilepsy surgery, and for whom the surgical outcome at least one year after surgery was known. The network was
124 based on the patient-specific [MEG connectivity](#). The model parameters were tuned using information about the
125 patient-specific seizure propagation patterns in invasive EEG recordings and the location of the resection area.
126 First, we showed that, despite its simplicity, the model provides a good approximation to clinically observed
127 seizure propagation patterns, and we fit the free parameters of the model to optimize the reproduction of the
128 individual seizures. Secondly, we used the individualized model to test alternative resection strategies and,
129 making use of an optimization algorithm, we found optimal – in terms of reduction of seizure propagation –
130 personalized resections.

131 2 Methods

132 2.1 Patient group

133 We retrospectively analyzed 10 patients (5 females) with refractory epilepsy (Table 1). All patients underwent
134 epilepsy surgery at the Amsterdam University Medical Center, location VUmc, between 2016 and 2019. All
135 patients had received a magnetoencephalography (MEG) recording, had undergone a SEEG (stereo-electro-
136 encephalography) study, and underwent pre- and post-surgical MR imaging. All patients gave written informed
137 consent and the study was performed in accordance with the Declaration of Helsinki and approved by the VUmc
138 Medical Ethics Committee.

139 The patient group was heterogeneous with temporal and extratemporal resection locations and different
140 etiology. Surgical outcome was classified according to the Engel classification at least one year after the operation
141 [59]. Patients with Engel class 1A were labelled as seizure free (SF), and patients with any other class were
142 labelled as non seizure free (NSF). 3 patients were deemed NSF.

143 2.2 Individualized Brain Networks

144 The individualized computer model was based on [the patient-specific](#) brain network (see figure 1) reconstructed
145 in the Brainnetome Atlas (BNA) from MEG scans, as detailed below. [We have considered the structural network](#)
146 [as the substrate for the propagation of ictal activity, in agreement with previous studies \[41\].](#) However, true
147 [structural networks \(e.g. DTI - Diffusion Tensor Imaging networks\)](#) cannot be derived from the scans that
148 [the patients get as part of their routine pre-surgical evaluation, and would thus require an extra imaging step,](#)
149 [increasing the personal and economic burden to apply the model clinically.](#) On the contrary, MEG scans are,
150 when available, part of the routine pre-surgical evaluation, and thus using MEG data to derive a surrogate

Patient	Sex	Age at Ep. Onset (y)	Duration of Ep. at Surgery (y)	MRI radiologic diagnosis	Pathology	Resection Area	S_{RA}	Engel Score	Surgery Outcome	#E	#ECP	N_{SR}
P1	F	20 – 29	10 – 19	normal MRI	mMCD-2	R-TL	5	2A	NSF	9	99	40
P2	M	20 – 30	10 – 19	normal MRI	mMCD-2	L-T	5	1A	SF	12	106	30
P3	F	40 – 50	30 – 39	normal MRI	mMCD-2	L-F	4	2C	NSF	13	117	47
P4	F	30 – 40	0 – 9	Multiple cavernoma	cavernoma & surrounding mMCD-2	L-T	5	1A	SF	11	110	44
P5	M	50 – 60	20 – 29	Post-traumatic gliosis	reactive changes	L-F	6	1A	SF	12	124	40
P6	F	20 – 30	10 – 19	normal MRI	mMCD-2	L-P	4	1A	SF	10	104	37
P7	M	20 – 30	10 – 19	FCD	mMCD-u	R-TPL, PL, PL	3	1A	SF	12	102	38
P8	F	50 – 60	20 – 29	normal MRI	FCD-2A	LT-MA	6	3A	NSF	15	194	60
P9	M	30 – 39	10 – 19	MTS	hippocampal sclerosis	RT-MA	12	1A	SF	10	107	32
P10	M	20 – 29	10 – 19	FCD	inconclusive	LI	6	1A	SF	14	193	49

Table 1: Patient data. Ep. = Epilepsy, y = years, S_{RA} = number of resected ROIs, #E = number of intracranial electrodes, #ECP = total number of electrode contact points, N_{SR} = number of BNA ROIs sampled by the SEEG electrodes. F = female, M = male, R = right, L = left, F = frontal, T = temporal, P = Parietal, TL = lateral temporal, TPL = posterior lateral temporal, PI = posterior insula, PL = posterior parietal, FCD = focal cortical dysplasia, mMCD = mild Malformation of Cortical Development, mMCD-2 = mMCD type 2, mMCD-u = mMCD type unknown, FCD-2A = focal cortical dysplasia type 2A, SF = seizure free, NSF = not seizure free.

151 for structural networks reduces the burden and increases the applicability of the model. This can be done
152 by considering a metric such as the uncorrected Amplitude Envelope Correlation (AEC). By not correcting
153 for the effects of volume conduction, this metric closely resembles the underlying brain anatomy and therefore
154 the structural connectivity. In order to validate the use of AEC-MEG networks as surrogate for structural
155 connectivity, we have compared them with a phenomenological model for structural connectivity the exponential
156 distance rule (EDR). This rule states that the weights of the connections between pairs of regions in the brain
157 decay exponentially with the distance between them [60–62], and has been repeatedly validated in human DTI
158 data [63–65]. In order to adapt this rule for the resolution of the BNA atlas (much lower than those used in
159 animal and human-DTI studies, which defined brain parcellations of millions of ROIs, instead of the 246 of the
160 BNA atlas), we computed the correlation between the network models for an array of decay-exponents, and
161 found the one yielding the best fit for the AEC-MEG networks.

162 Pre-operative Magnetic resonance imaging (MRI) scans were used for co-registration with the MEG data.
163 MRI T1 scans were acquired on a 3T whole-body MR scanner (Discovery MR750, GE Healthcare, Milwaukee,
164 Wisconsin, USA) using an eight-channel phased-array head coil. Anatomical 3D T1-weighted images were
165 obtained with a fast spoiled gradient-recalled echo sequence. During reconstruction, images were interpolated
166 to 1mm isotropic resolution.

167 2.2.1 MEG acquisition

168 MEG recordings were obtained during routine clinical practice using a whole-head MEG system (Elekta Neu-
169 romag Oy, Helsinki, Finland) with 306 channels consisting on 102 magnetometers and 204 gradiometers. The
170 patients were in supine position inside a magnetically shielded room (Vacuumshmelze GmbH, Hanau, Germany).
171 Typically, three data-sets of 10 to 15 minutes each containing eyes-closed resting-state recordings were acquired
172 and used in the presurgical evaluation for the identification and localization of interictal epileptiform activity.
173 Paradigms for the localization of eloquent cortex, such as voluntary movements and somatosensory stimulation
174 [66], as well as a hyperventilation paradigm to provoke interictal epileptiform discharges, were also recorded but
175 not analysed in this study. The data were sampled at 1250 Hz, and filtered with an anti-aliasing filter at 410 Hz
176 and a high-pass filter of 0.1 Hz. The head’s position relative to the MEG sensors was determined using the signals
177 from four or five head-localization coils that were recorded continuously. The positions of the head-localization
178 coils and the outline of the scalp (roughly 500 points) were measured with a 3D digitizer (Fastrak, Polhemus,
179 Colchester, VT, USA), and were later used for co-registration with the anatomical MRI.

180 The temporal extension of Signal Space Separation (tSSS) [67, 68] was used to remove artifacts using Maxfilter
181 software (Elekta Neuromag, Oy; version 2.1). The points on the scalp surface were used for co-registration with
182 the anatomical MRI of the patient through surface-matching software. A single sphere was fitted to the outline
183 of the scalp and used as a volume conductor model for the beamforming approach. For a detailed description
184 and parameter settings see [66].

185 2.2.2 MEG processing: Atlas-based Beamforming

186 Neuronal activity was reconstructed using an atlas-based beamforming approach, modified from [69], in which
187 the time-series of neuronal activation of the centroids of the ROIs were reconstructed [70]. We considered the
188 246 ROIs in the BNA atlas [71], including 36 subcortical ROIs, whose centroids were inversely transformed to
189 the co-registered MRI of the patient. Then, a scalar beamformer (Elekta Neuromag Oy; beamformer; version
190 2.2.10) was applied to reconstruct each centroid’s time-series. The beamformer weights were calculated for each
191 centroid separately to form a spatial filter so as to maximally let pass signals that originate from the centroid
192 of interest and to attenuate all other signals. The weights were based on the lead fields (using the spherical
193 head model and an equivalent current dipole as source model), the data covariance and noise covariance. The
194 broadband (0.5 – 48.0 Hz) data covariance was based on the entire recording (on average 799.23 seconds of data
195 (range: 309.50 - 908.67) were used). A unity matrix was used as noise covariance when estimating the optimum
196 source orientation for the beamformer weights [72]. The broadband data were projected through the normalised
197 beamformer weights [73] in order to obtain time-series (virtual electrodes, VE) for each centroid [70].

198 2.2.3 Brain Networks

199 The time-series for each VE were visually inspected for epileptiform activity and artifacts. On average, 53.1
200 (range: 19 – 60) interictal and artefact-free epochs of 16384 samples were selected for each patient. The epochs
201 were further analyzed in Brainwave (version 0.9.151.5 [75]) and were down-sampled to 312 Hz, both in the
202 broadband (0.5 - 48 Hz) and in the alpha-band (8 - 13 Hz).

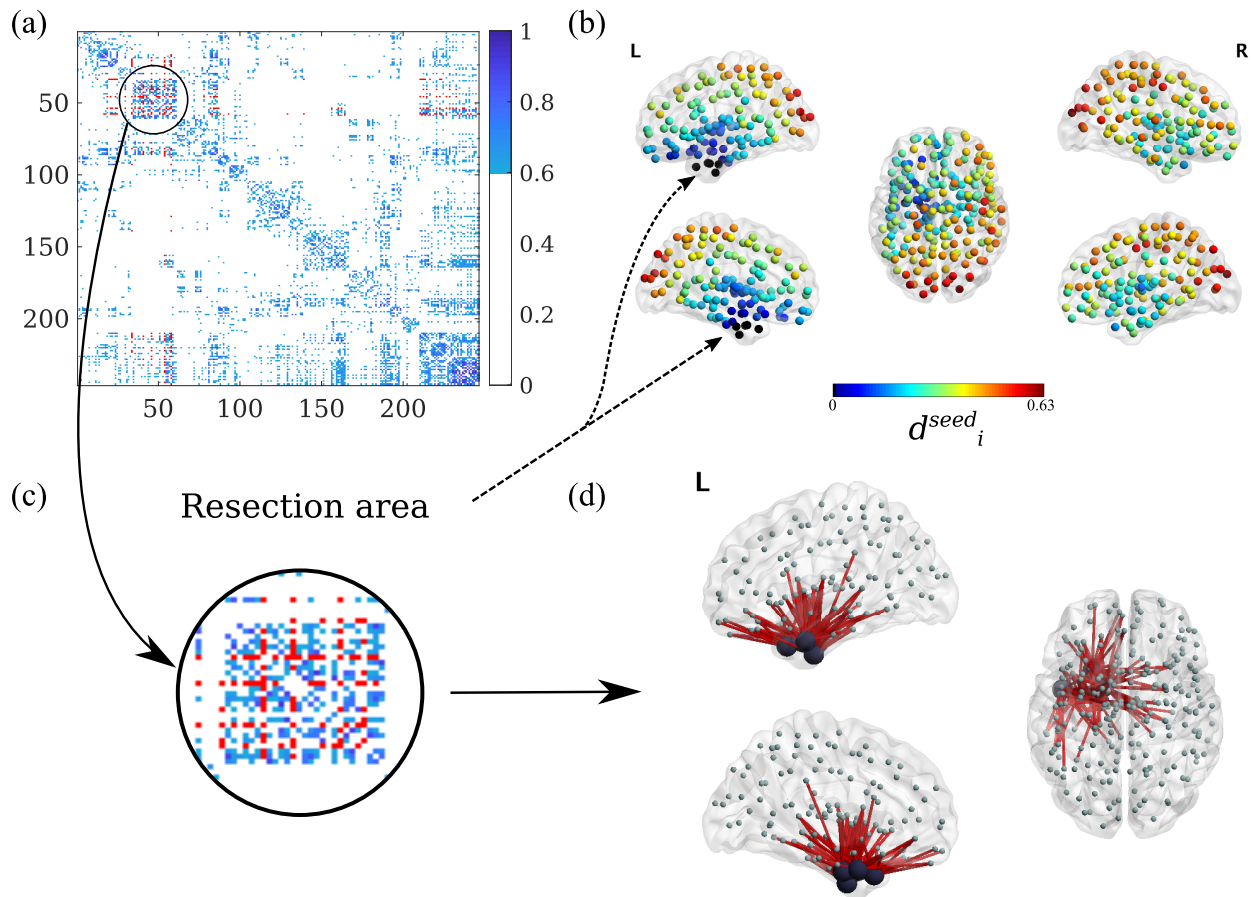


Figure 1: **Individual Brain Networks.** **a)** Weighted (and thresholded) resting-state broadband-MEG connectivity matrix for patient 4, for $\theta = 0.15$. Each entry corresponds to a BNA region, and the regions have been re-ordered to group regions in the same hemisphere. In this representation, ROIs 1-105 correspond to the left cortical regions, ROIs 106-210 to the right cortical regions and ROIs 211-246 to the subcortical regions (in alternating hemisphere order). The strength of each connection is indicated by the colorcode. In red we show the connections from and to the resection area (RA). **b)** Distribution of average distances to the RA according to eq.(S2) for patient 4, in dimensionless units. The points mark the centroids of the BNA ROIs, and the color scale indicates the effective distance of the ROI to the resection area (RA), which appears as black dots. **c)** Zoom-in of the adjacency matrix: RA and surrounding nodes. **d)** Illustrative representation of the RA (big black circles) and all the links connecting it with the rest of the network. Figures with brain representations have been obtained with the BrainNet Viewer [74].

Brain networks were generated using the 246 VEs as nodes (see figure 1a). Coupling strength (i.e. the elements w_{ij} of the weight matrices) was estimated by the AEC (Amplitude Envelop Correlation) [76–79]. The uncorrected AEC (i.e. without correcting for volume conduction) connectivity metric was selected as it maintains information on the structural connectivity pattern, whilst including information on long-range connections. AEC values range from 0 (no connectivity) to 1 [80]. The resulting networks were thresholded at different levels θ indicating the percentage of remaining links, and the resulting average connectivity $\kappa = \theta N$ of the network was determined. We considered a non-uniform grid in θ , with values $\theta = 0.01, 0.02, 0.04 \dots, 0.10, 0.15, \dots 0.50$, to account for the fact that the model is more sensitive to connectivity changes for small θ . Notice that the networks were thresholded but not binerized, so that w_{ij} remains a real variable ($w_{ij} \in [0, 1]$). The resulting weight matrix is represented in figure 1a for a characteristic case.

2.2.4 Resection Area

The resection area (RA) was determined for each patient from the three-month post-operative MRI. This was co-registered to the pre-operative MRI (used for the MEG co-registration) using FSL FLIRT (version 4.1.6) 12 parameter affine transformation, following previous studies [27, 30, 35, 36, 41, 44, 81]. The resection area was then visually identified and assigned to the corresponding BNA ROIs, name those that were overlapping for at least 50% with the resection area. Visual inspection confirmed that the co-registration was accurate and that any differences due to tissue adaptation after the surgery were small and at the sub-ROI level. In figure 1 we illustrate the resection area and its connectivity structure with the rest of the network for one patient.

2.3 Individualized Propagation Pattern

All patients underwent stereo-electroencephalography (SEEG) electrode implantation. The number and location of the intracerebral electrodes (Ad-Tech, Medical Instrument Corporation, USA, 10-15 contacts, 1.12 mm electrode diameter, 5 mm intercontact spacing; and DIXIE, 10-19 contacts, 0.8 mm electrode diameter, 2 mm contact length, 1.5 insulator length, 16 – 80.5 insulator spacer length) were planned individually for each patient by the clinical team, based on the location of the hypothesized seizure onset zone (SOZ) and seizure propagation pattern. Implantation was performed with a stereotactic procedure. The number of electrodes per patient varied between 9 and 15 (average = 11.8) and the total number of contacts between 99 and 194 (average = 125.6). Details of the number of electrodes and contact points for each patient are indicated in table 1.

The locations of the SEEG contact points were obtained from the post-implantation CT scan (containing the SEEG electrodes) that was co-registered to the preoperative MRI scan using FSL FLIRT (version 4.1.6) 12 parameter affine transformation (see figure 2a). Each electrode contact point (CP) was assigned the location of the nearest ROI mass center. Because BNA ROIs are in general larger than the separation between contact points, different CPs can have the same assigned ROI. We refer to the set of ROIs sampled by the SEEG CPs as $SEEG_{ROI}$, with the size of the set being N_{SR} (N_{SR} values for all patients are reported in table 1).

Based on the clinical recordings, a seizure propagation pattern was built indicating the order of activation of the electrode CPs for a typical seizure, as shown in figure 2b. In order to do so, the start of ictal activity of typical seizures was visually assessed for each SEEG CP by a clinician expert. Then, the CPs were grouped into activation steps according to when ictal activity was first observed. The seizure pattern was built from one typical seizure for each patient. This activation pattern was then translated into the BNA space (see figure 2b), so that the each ROI i in the sampled set $SEEG_{ROI}$ was assigned an activation step. Finally, we calculated the *activation rank* of each ROI in $SEEG_{ROI}$, such that the $SEEG_{ROI}$ ROIs were ordered and ranked according to their activation step, and groups with the same rank (i.e. in the same activation step) were assigned a rank equal to the midpoint of unadjusted values (see figure 2b). This yields the SEEG pattern $RANK_i^{SEEG}$ indicating the activation rank of each ROI i in $SEEG_{ROI}$.

2.4 Seizure Propagation Model

2.4.1 SI Dynamics

Seizure propagation was modelled via an epidemic spreading model: the susceptible-infected (SI) model [51]. This model depicts the propagation of an epidemic process on a network from a set of seed regions to the rest of the nodes. The model only accounts for the propagation process, as it does not include any mechanisms for the deactivation of the affected regions. It thus represents the initial steps of the propagation of a seizure, before inhibition takes place and the affected regions start to deactivate. Thus, we do not try to mimic the complicated processes involved in seizure generation and propagation with this model, which is used here as an

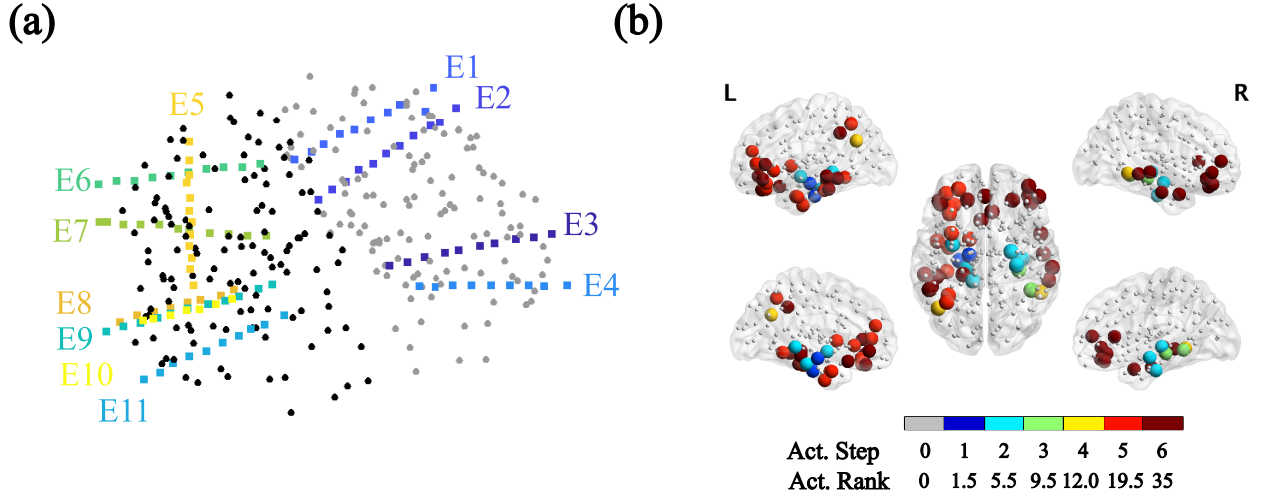


Figure 2: **Individualized Seizure Propagation Pattern.** **a)** SEEG electrodes for patient 4. Black and gray dots indicate the BNA ROIs' mass centers, respectively for the left and right hemispheres (different colors are used for visualization purposes). This patient had 11 intracranial electrodes implanted, each electrode is shown in a different color. **b)** Corresponding seizure pattern constructed from the clinical SEEG recordings. First, different activation steps were identified in the seizure recordings, together with the corresponding contact points (CPs). In the case depicted here, typical seizures consisted of 6 propagation steps, with step 1 depicting the seizure onset zone (as indicated by the SEEG recordings), and step 6 signalling the generalization of the seizure to all sampled CPs (note however that in general not all CPs need take part in the seizure propagation pattern). This propagation pattern was then translated into the BNA space, and the sampled ROIs are indicated here as large colored spheres. Thus, only the BNA ROIs sampled by the SEEG electrodes are included in the pattern, which in this case corresponded to a total of $N_{RS} = 49$ sampled ROIs (N_{RS} values for all patients are reported in table 1). The color code in the figure indicates the propagation step in which the corresponding CP is involved in ictal activity (i.e. Act. Step). Small grey dots mark the ROIs not included in the SEEG pattern. Finally, in order to enable comparison with the SEEG propagation pattern with the one modelled via the SI dynamics via the Mann-Whitney U test, we calculated the activation rank (Act. Rank) of each ROI, such that the ROIs were ordered and ranked according to the activation step, and groups with the same rank were assigned a rank equal to the midpoint of unadjusted values.

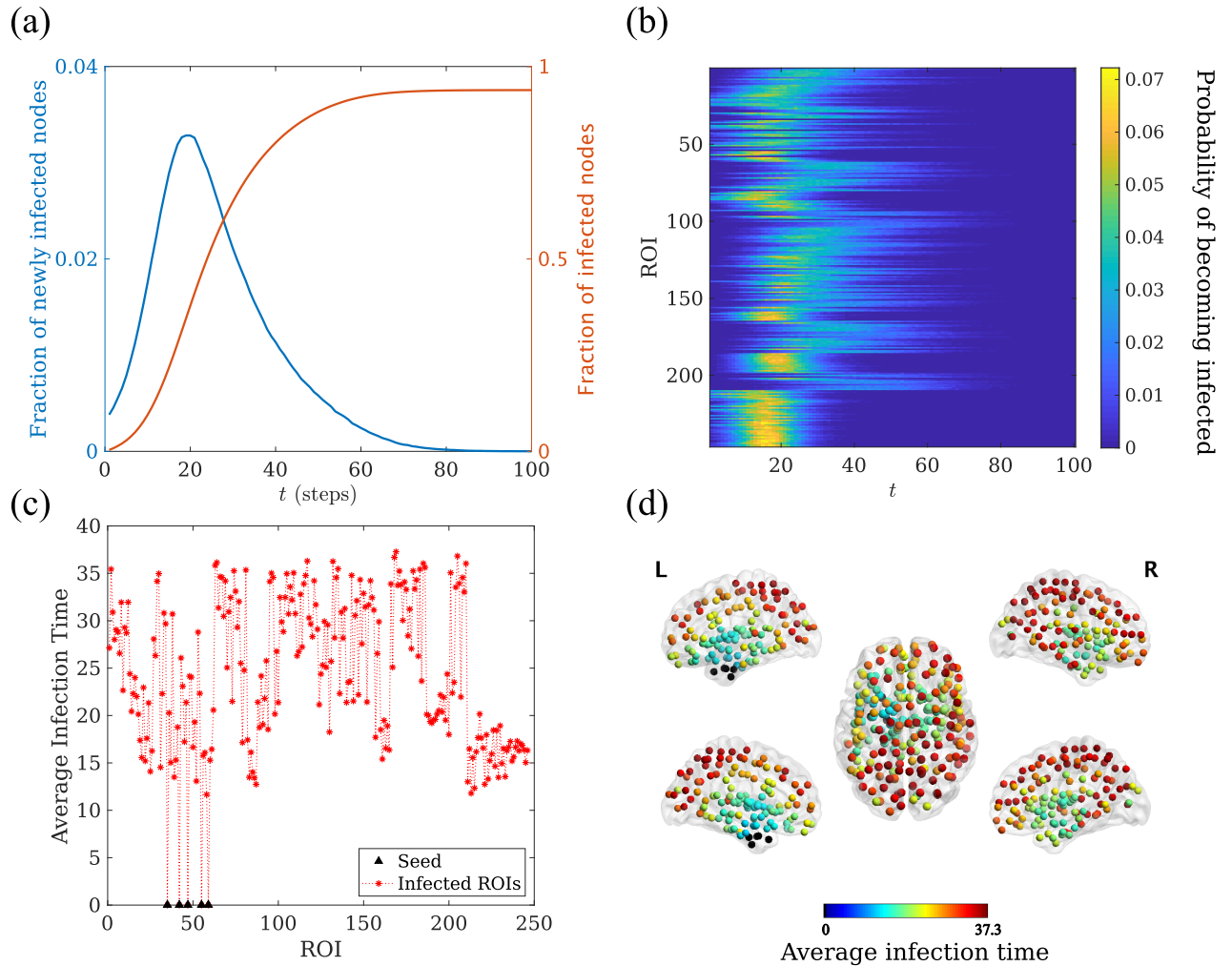


Figure 3: **Seizure propagation model.** Exemplary SI propagation process for patient 4. **(a)** $I(t)$ (red line) and the fraction of newly infected nodes at time t ($I(t) - I(t-1)$, blue line), as functions of time. **(b)** Model propagation pattern showing the probability $p_i(t)$, as indicated by the color scale, that a given ROI i (y-axis) becomes infected at time t (x-axis). **(c)** Average infection time for each ROI, t_i . The seed (corresponding to the resection area, shown in black triangles) is always infected at time 0. **(d)** Spatial representation of the ROIs mean infection time t_i . Each ROI is color-coded according to its average infection time. The resection area is shown as black circles. The time unit is the number of simulation steps in all panels.

abstraction that includes only the most relevant features of the initial steps of seizure propagation. Thanks to its simplicity, the model can be described by using only one parameter, the infection probability β , as described below. More complicated epidemic models, such as the SIR or SIS model [51], which include a deactivation mechanism, introduce more parameters that either have to be assumed or fitted with detailed data.

Simulation of the epidemics on the network takes place as follows. Each node is characterized by its state: either S (susceptible) or I (infected). Initially, all nodes are in the S state, except for a set of nodes in the I state, which act as the seed of the epidemic (or seizure). At each time step, each infected node can propagate the infection independently to any of its neighbours with probability βw_{ij} , where β characterizes the rate of the epidemic spreading and w_{ij} is the connection strength between nodes i and j as given by the MEG-AEC adjacency matrix. The fraction of infected nodes at each time is given by $I(t)$. If all nodes are connected, eventually the epidemic spreads over the whole network, $I(t \rightarrow \infty) = 1$, as shown in figure 3a. However, the speed and pattern of the propagation depend on β and w_{ij} (see figure 3).

In order to fit and validate the model, we first considered the situation of slow propagation in which only one new node is infected at each time step (formally corresponding to $\beta \rightarrow 0$), and compared the propagation pattern of the modelled epidemic process with the clinical SEEG seizure pattern for different connectivity thresholds θ . The threshold was then fit to maximize the correlation between the modelled and clinical propagation patterns. Then, to study the effect of different virtual resections, we quantified the short-term propagation of the seizure as the fraction of infected nodes at time t_0 . Here we set $t_0 = 50$ and, in order to account for different network densities, we set $\beta\theta = \text{const} = 4 \cdot 10^{-4}$ (so that $\beta = 0.01$ for a network with 4% of the links, for instance). For a standard resection size S_{RA} of 4 nodes this would correspond, in the uniform limit, to an infection of about 2/3 of the nodes [50].

SI dynamics was simulated in custom-made Matlab algorithms using Monte-Carlo methods, with $N_R = 10^4$ iterations of the algorithm for each configuration to assure convergence.

2.4.2 Optimization of SI parameters: Individualized Propagation Model

The SI dynamics were simulated as described above, leading to a probability map indicating the probability $p_i(t)$ that each ROI i became infected at step t , for each connectivity threshold θ , as shown in figure 3b. The mean activation time for each ROI was then calculated as $t_i = \sum_{t=0}^T p_i(t)$, where T is the maximum integration time. t_i describes the activation sequence of the ROIs during a modelled seizure (see figure 3c, d). Given that not all BNA ROIs were sampled by the SEEG electrodes, t_i was then sub-sampled to the SEEG_{ROI} set, and the included ROIs were ranked according to t_i . This ranking $\text{RANK}_i^{\text{SI}}$ constitutes the modelled or SI seizure propagation pattern, which is defined upon the same set of ROIs SEEG_{ROI} as the clinical one ($\text{RANK}_i^{\text{SEEG}}$), as shown in figure 4.

Once the SI pattern had been constructed, the ranked correlation was computed to compare the SI and SEEG patterns (see figure 4a) via a Mann-Whitney U test. The correlation is thus defined as

$$C = \frac{\text{cov}(\text{RANK}_i^{\text{SEEG}}, \text{RANK}_i^{\text{SI}})}{\sigma(\text{RANK}_i^{\text{SEEG}}) \sigma(\text{RANK}_i^{\text{SI}})} \quad (1)$$

where $\text{cov}(x, y)$ and $\sigma(x)$ respectively stand for the covariance and standard deviation. The connectivity threshold that maximized this correlation was independently found for each patient (see figure 4b) and used for the corresponding individualized virtual resection model.

Two possible seeds were considered for the SI dynamics: either the resection area (RA seed), or the hypothesized Seizure Onset Zone according to the SEEG clinical recordings (SOZ seed).

2.5 Simulation of Resections

Resections \mathcal{R} of sets of nodes were conducted in the model by the use of *virtual* resections (VRs). For this, all the connections of the corresponding nodes were set to 0, so the size of the network was left unchanged, but the resected nodes became isolated. Each resection \mathcal{R} was then characterized by measuring the fraction of infected nodes at a fixed time t_0 after the resection had taken place, $I_{\mathcal{R}}(t_0)$ (see figure 5).

The goal of epilepsy surgery is to completely stop seizure propagation ($I_{\mathcal{R}}(t_0) \rightarrow 0 \forall t_0$) which, in the present model, can only be attained by (and it is always attained by [82, 83]) complete disconnection of the assumed seed region. Thus, in this study the effect of each resection was measured in terms of the decrease in the speed of seizure propagation, and the goal was to find the smallest resection able to reduce the initial propagation at t_0 by 90%. That is, to find the smallest resection such that $i_{\mathcal{R}} = I_{\mathcal{R}}(t_0)/I(t_0) \leq 0.1$, where $I(t_0)$ is measured on the original pre-resection network [41].

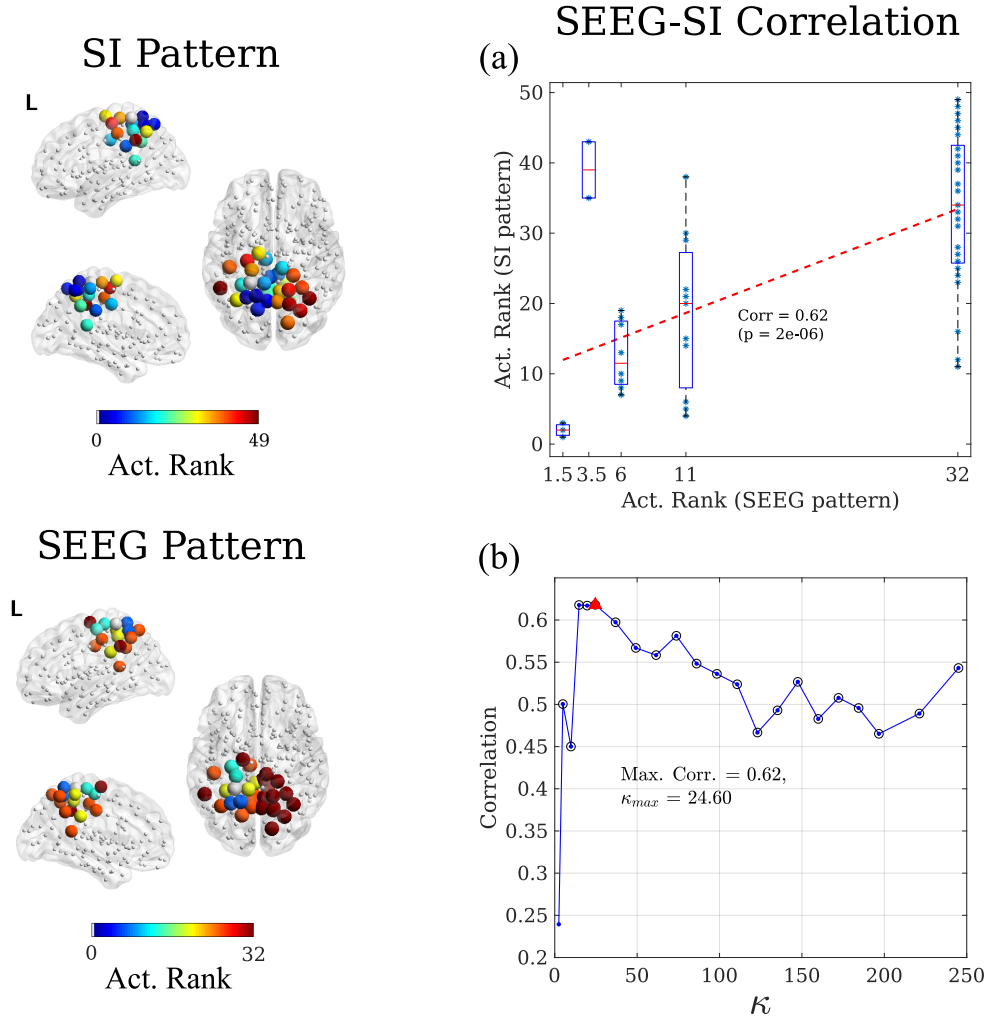


Figure 4: **Correlation method.** Here we illustrate, for patient 3, the correlation method to validate and fit the seizure propagation model. For each network connectivity threshold θ , the SI dynamics was simulated over the whole MEG network, and the propagation pattern was constructed for the ROIs sampled by the SEEG electrodes and compared with the clinical SEEG pattern. Each pattern describes the activation order – or rank – of each sampled ROI. Given that the clinical SEEG pattern is built in term of activation steps, different ROIs can have the same ranking, as described in the main text. The modelled SI pattern was correlated with the clinical SEEG pattern, as depicted in panel (a). This process was iterated for different connectivity thresholds θ leading the correlation curve shown in panel (b), where the mean degree $\kappa = \theta N$ is shown in the x-axis, and significant correlations are indicated with a black circle. Finally, the connectivity leading to the maximum correlation was chosen. In the depicted case, this corresponded to a mean degree of $\kappa = 24.60$ ($\theta = 0.1$) leading a correlation of 0.62 (red triangle). This also corresponds to the value of κ used for panel a.

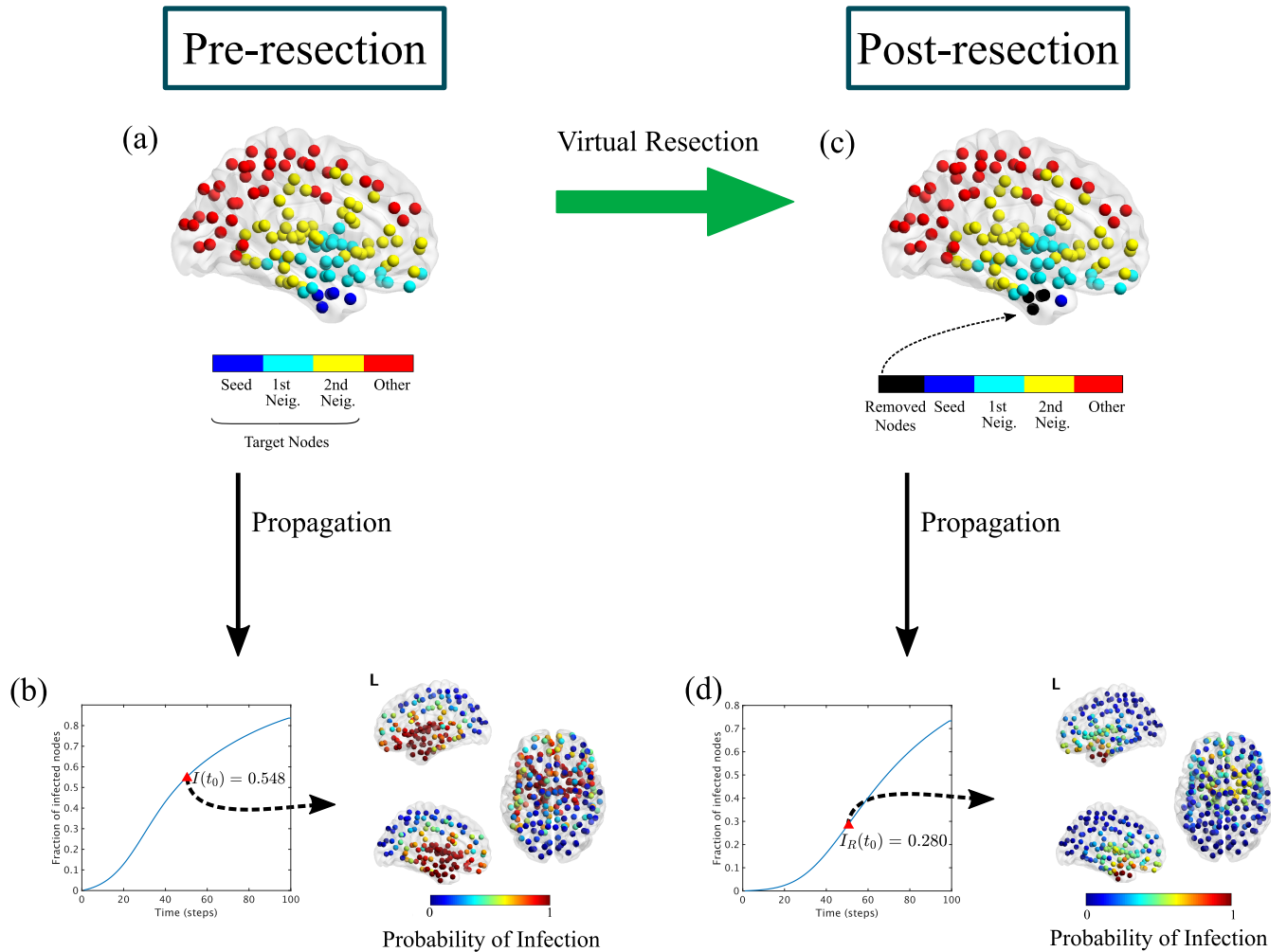


Figure 5: **Virtual Resection Implementation.** The target nodes for the virtual resection VR are all nodes at two steps or less from the seed, i.e. the seed and its first and second neighbours (panel **a**). The initial seizure propagation is the fraction of infected nodes at $t_0 = 50$, $I(t_0) = 0.548$ (panel **b**). A virtual resection of 5 nodes is implemented in the network by setting to 0 all the links with the corresponding nodes, marked in black in panel **c**. Seizure propagation is now reduced by approximately a factor 2 ($I_R(t_0) = 0.280$), and the probability that the seizure reaches regions outside the seed decreases considerably (panel **d**). This example corresponds to patient 4.

We defined a four-step method to find the optimal resection \mathcal{R}^* for each resection size S , $\mathcal{R}^*(S)$. That is, the resection leading to a minimum propagation $I_{\mathcal{R}^*(S)}(t_0)$. The optimization method made use of the Simulated Annealing algorithm [84] to speed up the exploration of the space of possible resections, and it considered a surrogate structural metric – the mean *effective distance* to the seed [50, 57, 58] – as a proxy for the SI dynamics to simplify the initial exploration (the method and algorithms used are described in detail in the Supplementary Information and figure S1). Then, the smallest resection leading to a 90% reduction in seizure propagation (as measured by $I_{\mathcal{R}}(t_0)$), \mathcal{R}_{90} , was identified. We also identified, for each patient, the smallest resection leading to 100% reduction in propagation ($I_{\mathcal{R}}(t_0) = 0$), \mathcal{R}_{100} . Finally, to characterize the effect of small resections in seizure propagation, we also defined the one-node resection, \mathcal{R}_1 , as the resection of size 1 with a maximum effect.

In principle all nodes in the network could be considered as possible targets to be resected. However, the effect of each node on seizure propagation decreases as it gets further from the seed (in terms of hops on the network). Therefore, here we considered only nodes that were at most two hops (without taking into account the edge weights) away from the seed (that is, the seed and its first and second neighbours), as depicted in figure 5a.

2.6 Statistics

The comparison between network matrices was done via the Pearson’s correlation coefficient, calculated over the 1-dimensional vector of connectivity (i.e. by stacking all matrix-connectivity columns one after the other).

The Mann-Whitney U test was used to determine the correlation between the modelled and clinical seizure propagation patterns. To compare the optimal correlation obtained with different network definitions we used a paired Student’s t-test. Similarly, different seed definitions were compared using a paired Student’s t-test. Finally, for comparisons between SF and NSF patients, we used an unpaired Student’s t-test. All significance thresholds were set at $p < 0.05$.

Finally, analyzed the effect of the size and mean degree of the resection area on the size of the 90% and 100% resections, and on the effect of the one-node resection, with a linear least squares fit.

2.7 Data availability

The data used for this manuscript are not publicly available because the patients did not consent for the sharing of their clinically obtained data. Requests to access to the datasets should be directed to the corresponding author. All user-developed codes are available from the corresponding author upon reasonable request.

3 Results

3.1 Preliminary results

A total of 10 patients (5 females) were included in the study, 7 of whom were deemed SF one year after surgery (see table 1 for the patient details).

We obtained the individual weighted AEC-MEG connectivity networks, with entries w_{ij} characterizing the coupling strength between ROIs i and j , for each patient in the alpha-band and the broad-band using the BNA atlas (246 nodes). The tables and figures shown in the main text report the results for the broad-band networks, details for the alpha-band can be found in the Supplementary Information. An exemplary matrix is shown in figure 1. We found that the broad-band MEG-AEC networks were a good surrogate for structural connectivity, with an average correlation of 0.51 ± 0.06 when considering the literature-based decay exponent (equal to -0.188) and of 0.71 ± 0.08 when considering a modified exponent to fit this atlas resolution (-0.052).

We constructed a clinical propagation pattern from the seizures observed with SEEG, for each patient. The pattern was initially defined in term of the electrodes CP, and then translated into the ROIs of the BNA atlas (see figure 2).

3.2 Reproduction of Seizure Propagation Patterns

As described in the methods section (see figure 4), we estimated the correlation C between the SI seizure pattern and the SEEG pattern for a range of connectivity values κ , as shown in figure 6a for the broadband networks and in figure S3 for the alpha-band networks. Then, to fit the spreading model to the SEEG propagation data, we selected the connectivity value κ_{\max} that maximized $C(\kappa)$, for each patient. The maximum correlation C_{\max} obtained for each patient and the corresponding κ_{\max} are shown in figure 7a,b for the broadband networks

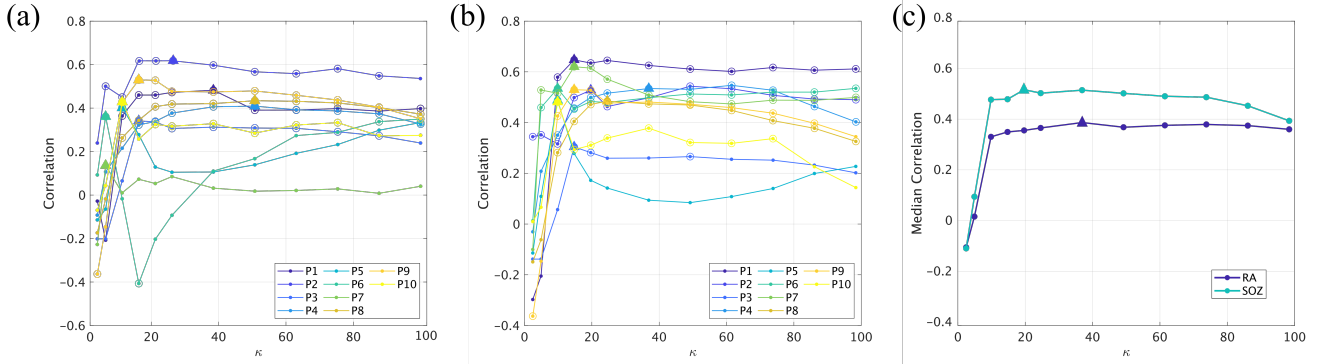


Figure 6: **Reproduction of seizure propagation.** Correlation between the modelled and clinically observed seizure propagation patterns as a function of network density, for each patient, using the RA (panel a) and SOZ seeds (panel b). Panel (c) indicates the median curves for each case, as indicated by the legend. Circles in panels a and b denote significant correlations ($p < 0.05$), and the optimal correlation for each case is marked with a triangle.

and in figure S4 for the alpha-band networks, and the corresponding values are reported in tables S1 and S2, respectively. Most cases presented a bimodal dependence of the correlation on the network density, so that there was a maximum for low density and another maximum for large density. Here we restrict our analyses to the first maximum, which yields only the fundamental connections that are needed to reproduce seizure propagation.

We found that the model significantly reproduced the seizure propagation patterns for 9/10 patients. The average correlation was $C^\alpha = 0.38$ for the alpha-band (α) networks and $C^{\text{BB}} = 0.41$ for the broad-band (BB) networks. The difference between the two settings (0.03, $\text{BB} > \alpha$) was not significant ($t(9) = 1.81$, $p = 0.06$). There were no significant differences in the optimal correlation between SF and NSF patients ($C_{\text{SF}}^\alpha - C_{\text{NSF}}^\alpha = -0.05$, $p = 0.3$, $t(8) = -0.41$; $C_{\text{SF}}^{\text{BB}} - C_{\text{NSF}}^{\text{BB}} = -0.01$, $p = 0.5$, $t(8) = -0.07$, unpaired Student t-tests). The optimal network density did not differ significantly between frequency bands ($\kappa^{\text{BB}} - \kappa^\alpha = 0.99$, $p = 0.4$, $t(9) = 0.15$) or between the sub-groups ($\kappa_{\text{SF}}^\alpha - \kappa_{\text{NSF}}^\alpha = 13.47$, $p = 0.05$, $t(8) = 1.91$; $\kappa_{\text{SF}}^{\text{BB}} - \kappa_{\text{NSF}}^{\text{BB}} = -16.75$, $p = 0.09$, $t(8) = -1.50$).

3.2.1 Alternative Definition of the Seed

Different definitions of the seed can be considered. So far, we used the resection area, but in prospective studies the actual resection area will not be known. We therefore also considered the SOZ, as defined by the SEEG study, as the seed for the SI spreading (seed SOZ), and repeated the fit method as before (see figure 6b). We found that now the correlation between the model and the seizure pattern was significant for all patients, both for the alpha- and broad-band networks. The average correlations were respectively $C^\alpha = 0.47$ and $C^{\text{BB}} = 0.51$. The difference ($C^\alpha - C^{\text{BB}} = -0.04$) was significant ($p = 0.04$, $t(9) = -1.99$).

We found that the optimal correlation was higher for SF than for NSF patients ($C_{\text{SF}}^\alpha - C_{\text{NSF}}^\alpha = 0.06$, $C_{\text{SF}}^{\text{BB}} - C_{\text{NSF}}^{\text{BB}} = 0.05$), although the difference was not significant (for α -networks: $p = 0.2$, $t(8) = 0.79$; for BB networks: $p = 0.2$, $t(8) = 0.79$). The optimal network density did not differ significantly between frequency bands ($\kappa^{\text{BB}} - \kappa^\alpha = -6.64$, $p = 0.08$, $t(9) = -1.52$) or between the sub-groups ($\kappa_{\text{SF}}^\alpha - \kappa_{\text{NSF}}^\alpha = 6.80$, $p = 0.2$, $t(8) = 0.79$; $\kappa_{\text{SF}}^{\text{BB}} - \kappa_{\text{NSF}}^{\text{BB}} = -1.51$, $p = 0.4$, $t(8) = -0.25$).

Overall, this seed definition reproduced the clinical seizure pattern better than the RA seed ($C^\alpha(\text{SOZ}) - C^\alpha(\text{RA}) = 0.09$, $p = 0.07$, $t(9) = 1.63$; $C^{\text{BB}}(\text{SOZ}) - C^{\text{BB}}(\text{RA}) = 0.10$, $p = 0.04$, $t(9) = 1.99$), although the difference was only significant for broad-band networks.

3.2.2 Effect of Individualized Brain Networks

Is patient specific connectivity required to reproduce the clinically observed seizure propagation patterns? In order to answer this question, we repeated the analysis using the average connectivity matrix (referred to as AV- α and AV-BB respectively for the alpha-band and broadband networks) as the network backbone for the SI spreading dynamics for all patients.

For the broad-band network, a significant correlation was found for 8 (10) patients using the RA (SOZ) seed (see figures 7 and S4). The average optimal correlation ($C^{\text{AV-BB}}(\text{RA}) = 0.36$, $C^{\text{AV-}\alpha}(\text{SOZ}) = 0.48$) was smaller than for the individual patient networks ($C^{\text{BB}}(\text{RA}) - C^{\text{AV-BB}}(\text{RA}) = 0.05$, $p = 0.08$, $t(9) = 1.95$; $C^{\text{BB}}(\text{SOZ}) - C^{\text{AV-BB}}(\text{SOZ}) = 0.03$, $p = 0.09$, $t(9) = 1.92$), although the difference was not significant. For the alpha-band network, a significant correlation was found for 7 (10) patients using the RA (SOZ) seed. The average (optimal) correlation ($C^{\text{AV-}\alpha}(\text{RA}) = 0.34$, $C^{\text{AV-}\alpha}(\text{SOZ}) = 0.46$) was smaller than for the individual patient networks ($C^{\alpha}(\text{RA}) - C^{\text{AV-}\alpha}(\text{RA}) = 0.05$, $p = 0.2$, $t(9) = 1.30$; $C^{\alpha}(\text{SOZ}) - C^{\text{AV-}\alpha}(\text{SOZ}) = 0.01$, $p = 0.8$, $t(9) = 0.28$) but the difference was not significant.

3.2.3 Average model

Above, the optimal network connectivity was fitted independently for each patient using the SEEG data. In order to test if a mean model could be used for patients without SEEG recordings, we have estimated the median correlation yielded by the model for each connectivity value, as depicted in figure 6c for BB-networks and figure S3c for α -band networks, both for the RA and SOZ seeds. For BB-networks, the maximum overall correlations found were $C_m^{\text{BB}}(\text{RA}) = 0.37$ for $\kappa = 36.90$ for the RA seed; and $C_m^{\text{BB}}(\text{SOZ}) = 0.49$ for $\kappa = 19.68$ for the SOZ seed. For α -band networks, the maximum overall correlations found are $C_m^{\alpha}(\text{RA}) = 0.33$ for $\kappa = 19.68$ for the RA seed; and $C_m^{\alpha}(\text{SOZ}) = 0.45$ for $\kappa = 19.68$ for the SOZ seed. These values were smaller than the mean optimal results ($C^{\text{BB}}(\text{RA}) = 0.41$, $C^{\text{BB}}(\text{SOZ}) = 0.51$, $C^{\alpha}(\text{RA}) = 0.38$, $C^{\alpha}(\text{SOZ}) = 0.47$), but the decrease was less than 15% on average and not significant ($t(9) = 1.95$, $p = 0.08$ and $t(9) = 1.90$, respectively for the α -band and BB networks).

3.2.4 Comparison with Fully Connected Networks

We also compared the correlation results with those obtained using a trivial fully connected network. Correlation results for this structure are shown in figures 7 and S4, together with the results obtained with individual broad-band networks (averaged) and when using the average broad-band network. Although the fully connected network achieved a significant correlation for some patients (3 patients for the RA seed and 5 for the SOZ seed), the correlation was always lower than for the individually optimised model, except for one patient using the SOZ seed, and the average was significantly smaller ($C^{\text{BB}}(\text{RA}) - C^{\text{FCN}}(\text{RA}) = 0.29$, $p = 1.4 \cdot 10^{-4}$, $t(9) = -6.27$; $C^{\text{BB}}(\text{SOZ}) - C^{\text{FCN}}(\text{SOZ}) = 0.22$, $p = 0.005$, $t(9) = 3.72$; $C^{\alpha}(\text{RA}) - C^{\text{FCN}}(\text{RA}) = 0.27$, $p = 7 \cdot 10^{-4}$, $t(9) = 5.01$; $C^{\alpha}(\text{RA}) - C^{\text{FCN}}(\text{SOZ}) = 0.18$, $p = 0.013$, $t(9) = 3.09$).

3.3 Virtual Resection Analysis

We made use of the VR optimization method illustrated in figures 5 and S1 to find optimal virtual resections of increasing size S , for each patient. Results of the virtual resection analysis are shown in figure 8 for all patients. Propagation after the resection (as measured by $I_{\mathcal{R}}(t_0)$) decreased as S increased for all patients. However, the exact trend that was followed depended on the individual network structure and seed size. Patients 3, 5 – 7 showed a rapid decrease of $I_{\mathcal{R}}(t_0)(S)$ for small S , whereas patient 9 showed a slower (parabolic) decrease. The remaining patients showed approximately linear decreases.

Complete stop of seizure propagation was found for the trivial resection of size $S = S_{\text{RA}}$, which corresponds to complete removal of the seed, for all patients. However, in some cases the 100% resection \mathcal{R}_{100} (i.e. the smallest resection leading to a 100% decrease in seizure propagation) was smaller than resection area. This resection is indicated by black squares in figure 8. We found that \mathcal{R}_{100} was smaller than the resection area for 4 patients (patients 4, 6, 7 and 10). Moreover, for 7/10 patients we were able to find a resection \mathcal{R}_{90} , of smaller size than the actual resection, yet that achieved over 90% decrease in propagation, as indicated by red triangles in figure 8. The sizes of the \mathcal{R}_{90} and \mathcal{R}_{100} resections relative to the size of the resection area, i.e. $s_{90} = S_{\mathcal{R}_{90}}/S_{\text{RA}}$ and $s_{100} = S_{\mathcal{R}_{100}}/S_{\text{RA}}$, are shown in figure 9a for all patients. On average, s_{90} was 74% (range: 33 – 100%), whereas the s_{100} was 90% (range: 67 – 100%).

The $I_{\mathcal{R}}(S)$ curves shown in figure 8 indicate that, for some patients, performing just a one-node resection, \mathcal{R}_1 , already had a large effect on (reducing) seizure propagation. This is explicitly shown by $i_{\mathcal{R}_1} = I_{\mathcal{R}_1}(t_0)/I(t_0)$ in figure 9b. The average effect of the 1-node resection was a 58% reduction in seizure propagation, although this number varied greatly among patients (range: 4–97%).

We analyzed the effect of the seed size and its connectivity on these results (see Supplementary Information, figure S5) by correlating s_{90} , s_{100} and $i_{\mathcal{R}_1}$ respectively with the number of links with nodes that were in the resection area, $E_{\text{RA}} = S_{\text{RA}} * \kappa_{\text{RA}}$. We found that s_{90} and s_{100} correlated positively with E_{RA} ($r(8) = 0.81$, $p = 0.005$ and $r(8) = 0.61$, $p = 0.07$, for s_{90} and s_{100} , respectively), although the correlation was only significant

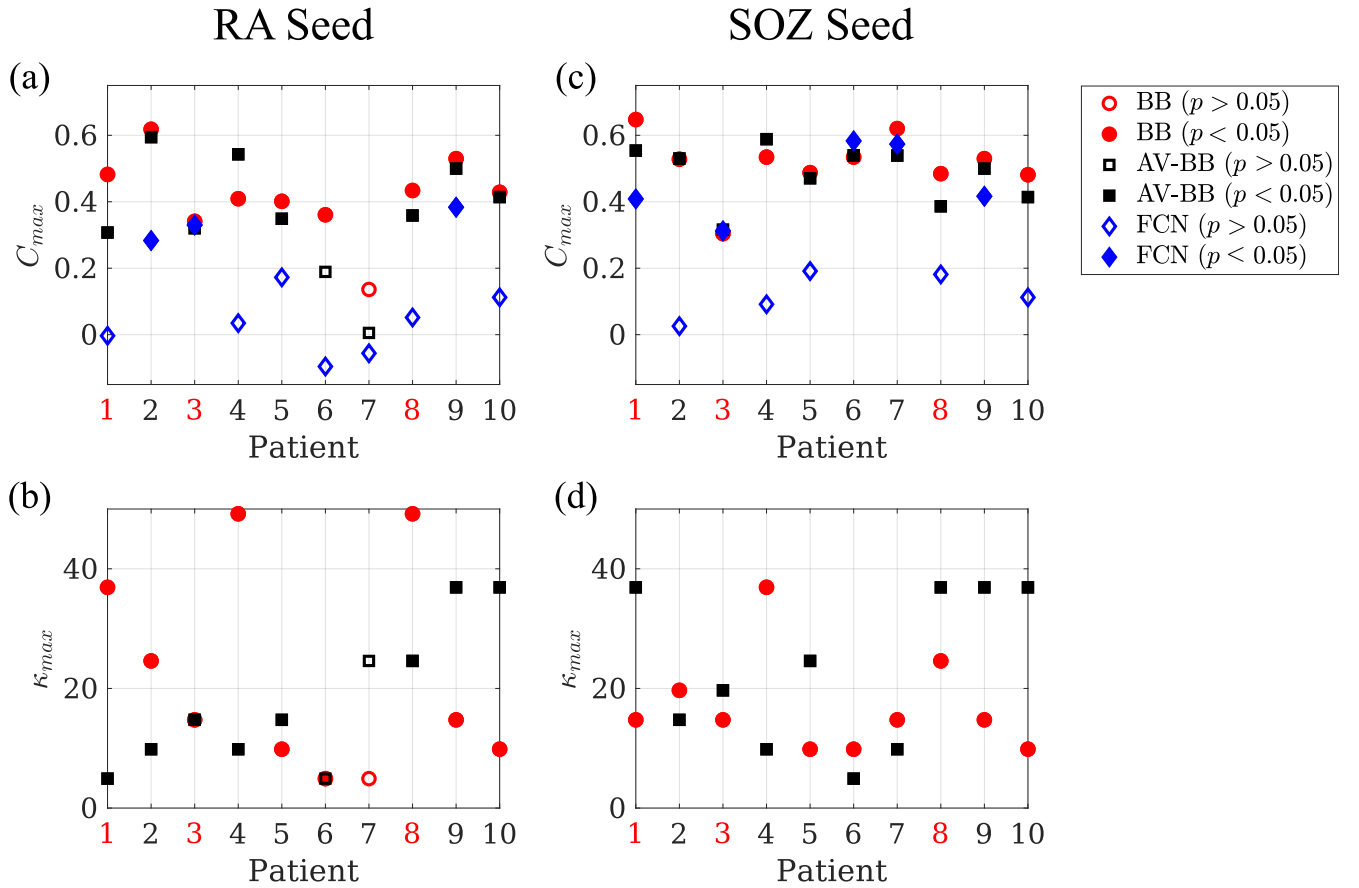


Figure 7: **Reproduction of seizure propagation patterns.** Panels (a) and (c) show the average maximum correlation C_{max} achieved by the individual BB networks (BB, red circles), and the average BB one (AV-BB, black squares), and the correlation found for the fully connected network (FCN, blue diamonds), respectively for the RA and SOZ seeds. Panels (b) and (d) show the corresponding κ_{max} for the individual (BB, red circles) and average (AV-BB, black squares) networks. Significant correlations ($p < 0.05$) are indicated by a filled marker, and non-significant ones ($p > 0.05$) by an empty marker. NSF patients are indicated by red labels.

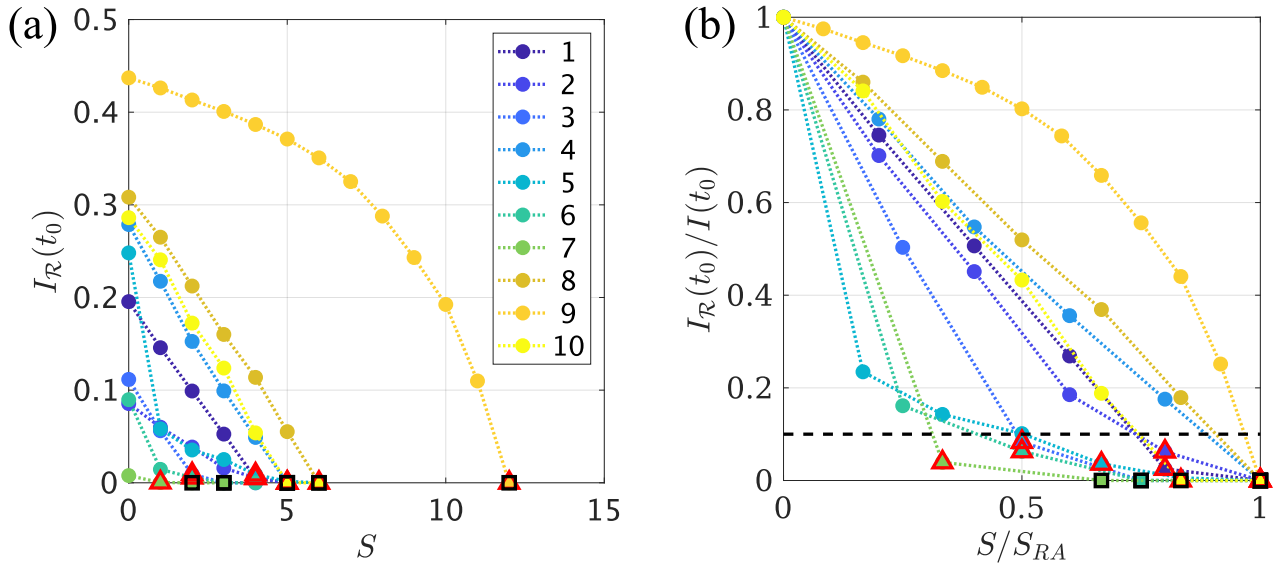


Figure 8: **Optimal Virtual Resection.** (a) Reduction in epidemic spreading for virtual resections of increasing size S , as quantified by the decrease in $I_{\mathcal{R}}(t_0)$. Each curve corresponds to one patient, as indicated in the legend. Red triangles mark the resection that achieved a 90% decrease in propagation, \mathcal{R}_{90} , and black squares the smallest resection that stopped seizure propagation, \mathcal{R}_{100} . (b) In order to enable comparison of the VRs performance between patients, we depict the normalized decrease in propagation, $I_{\mathcal{R}}(t_0)/I(t_0)$ as a function of the normalized resection size, S/S_{RA} . The black dashed line indicates a 90% decrease in propagation.

436 for s_{90} . On the contrary, $i_{\mathcal{R}1}$ correlated negatively with E_{RA} ($r(8) = -0.71$, $p = 0.02$). These results indicate
 437 that larger seed regions required a comparatively larger resection.

438 Finally, we analysed the location of the optimal resections found by the model (data not shown). We found
 439 that, for 1 patient, the optimal resection \mathcal{R}_{90} included nodes outside of the resection area and, similarly, \mathcal{R}_{100}
 440 was also found to include nodes outside of the resection area for another patient.

441 4 Discussion

442 We have defined a patient-specific seizure-propagation model based on the SI spreading dynamics. The model
 443 considers the patient-specific **AEC-MEG connectivity** matrix and makes use of clinical SEEG data to define
 444 stereotypical seizure propagation patterns for each patient. Seizure propagation was then modeled as an SI
 445 process propagating from a seed – which we initially took to be the patient’s resection area (RA) – to the rest of
 446 the network. Comparing the propagation patterns in the model to those observed clinically, we showed that this
 447 simple model reproduces the main aspects of the individual seizure propagation patterns, and that an alternative
 448 definition of the seed – based on the SEEG recordings – might provide a better reproduction of the observed
 449 propagation patterns. The main free parameter of the model – the network mean connectivity – was fitted to
 450 maximally reproduce the clinical seizure pattern, independently for each patient.

451 Using the model settings that optimally reproduced the clinically observed patterns, we then made use of
 452 the virtual resection technique to study alternative resections of smaller size or at different locations relative
 453 to the clinical resection area. The model suggested smaller virtual resections that were usually confined to the
 454 resection area, but in some cases included regions outside of the resected area.

455 4.1 Modeling Considerations

456 In this study we considered how individualized computer models, integrating patient-specific data from different
 457 modalities, can aid epilepsy surgery [26, 32–40, 42, 43, 85]. As opposed to previous studies which considered
 458 highly detailed, non-linear, stochastic models to simulate the activity of each brain region in detail [35, 37, 40,
 459 43, 86–88], here we considered an abstract model of epidemic spreading, the SI model, as a proxy for seizure
 460 propagation dynamics (see figures 3 and 4). Epidemic models capture the basic mechanisms of processes that

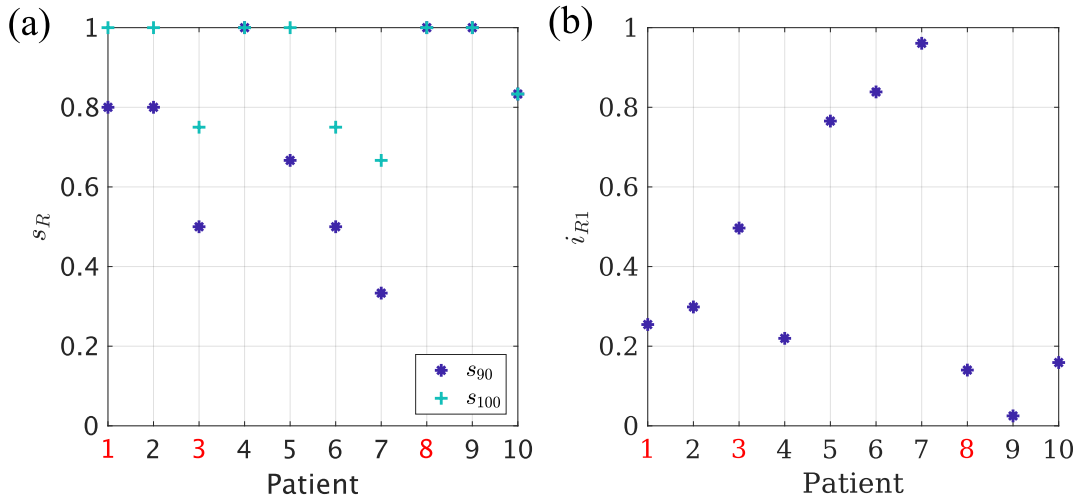


Figure 9: **Analysis of optimal virtual resections.** (a) Normalized size of the 90% (s_{90} , dark blue asterisks) and 100% (s_{100} , turquoise crosses) resections for each patient. (b) Normalized effect $i_{R1} = I_{R1}(t_0)/I(t_0)$ of the one node resection, for each patient. NSF patients are indicated by red labels in both panels.

diffuse on networked systems, and have been used, for example, to study the propagation of pathological proteins on brain networks [52] and of ictal activity [41].

Moreover, epidemic models are supported by a well-grounded mathematical framework that can aid the exploration of the model. For instance, the fundamental role of hubs in seizure propagation is expected from a spreading perspective: hubs can act as super spreaders, being responsible for a disproportionate number of infections [54, 89], and their existence enhances epidemic spreading, both increasing the speed of propagation and decreasing the epidemic threshold [51]. On the contrary, a strong community structure can help control the epidemic, which may remain trapped in one community [90, 91]. This result also aligns with the clinical observation that often seizure propagation can be restricted to one or a few brain lobes [1], in the case of focal epilepsy. This is characterized by focal seizures that remain within some regions and only sometimes brake through the inhibitory “wall” and generalize. Interestingly, seizures originating in certain regions (such as the temporal lobes) are more likely to remain focal than others (such as frontal seizures). Similarly, other network characteristics such as temporal changes in connectivity [92, 93] or degree correlations can also alter behavior of spreading processes [94].

Epidemic models can thus help us studying seizure propagation processes. Of the large family of such models, we have selected the SI model as it captures the basic nature of epidemic spreading processes, including seizure propagation [51]. It only considers one mechanism: the propagation of an infectious process (or a seizure) from one region to another. Consequently, there is only one free parameter in the model – the probability that the infection is transmitted. This comes at the cost of not allowing for region deactivation: the model can only describe the initial steps of seizure propagation, when the activity starts to spread out. More detailed propagation models – such as the Susceptible-Infected-Susceptible (SIS) or Susceptible-Infected-Recovered (SIR) models – do include deactivation mechanisms, but in doing so extra parameters are introduced that would need to be fine tuned or assumed upon. Moreover, the early propagation-dominated phase of the SIR model is highly similar to the SI model, and this is the regime of interest here.

As the backbone for seizure propagation in the model, we used the broad-band [AEC-MEG connectivity network](#) as a proxy for the structural brain network (see figure 1). By not correcting for the effect of volume conduction/field spread, short-range connections are present in the network [76–79], yet it also captures long-range connections that might be difficult to capture with DTI-based tractography. [We validated the use of AEC-MEG networks as surrogate for structural connectivity by comparing them with the structural connectivity model of the exponential-distance rule \(EDR\), and we found a high correlation between the two network descriptions.](#) Moreover, the [AEC-MEG network](#) is a good indicator of how activity spreads on the network and, as we have shown, it suffices to reproduce the SEEG seizure propagation patterns when used in combination with the SI model.

4.2 Reproduction of seizure propagation patterns

In many patients, seizures follow stereotypical activation patterns. In this study we selected 10 patients who showed clear patterns on the SEEG recordings (see figure 2), and compared seizure propagation in the model with those clinically observed patterns, as depicted in figure 4. Despite its simplicity, we found that the model reproduces the main characteristics of the individual seizure propagation patterns in 9/10 patients when the resection area was considered as the seed (see figures 6a and 7a,b). Moreover, by using the possible seizure onset zone, as indicated by the SEEG recordings, as the seed for epidemic spreading, we showed that the model is sensitive to different definitions of the seed, and that alternative definitions can improve on the reproduction of the clinical patterns (see figures 6b and 7c,d). We also found that patient specific connectivity reproduces seizure propagation better than fully connected networks, and marginally (although not significantly) better than the average connectivity network (see figure 7). This result is in line with previous studies [36, 41] in which possible benefits of using patient-specific connectivity were suggested, but could not be corroborated by a significant difference in the model. Likely, larger data sets would be necessary to unravel how the models benefit from considering patient-specific connectivity.

The density of connections of the network was set for each patient to fit the SEEG seizure propagation pattern. Higher density levels imply a more extended or homogeneous propagation pattern, whereas smaller ones are associated with a more well-defined propagation. Then, the SI propagation rate β was adjusted accordingly for each patient for the subsequent virtual resection analysis.

The model parameters were fitted to the patient’s SEEG data, hence the current definition of the model relies on the use of SEEG recordings to infer the patient-specific seizure-propagation patterns and fit the model free parameters. However, these are not always part of standard clinical practice, as they are highly invasive for the patient and not always needed during pre-surgical planning. In order to show the feasibility of applying the model to patients without such recordings, we have shown in figure 6c that the average optimal model parameters can be used as an approximate solution. The propagation of seizures typically makes use of existing pathways, many of which are not patient-specific and can be recovered by the average model parameters. In the current setting, considering the overall best threshold for the connectivity matrix, instead of the individual one, led to less than a 15% decrease in correlation between the modeled and clinical seizure-propagation patterns. Within this configuration, the model is still personalized, as it is still fitted specifically for each patient via the patient’s MEG based connectivity matrix and seed for the SI propagation dynamics. Moreover, if a larger data-base is constructed, the patients could be grouped by epilepsy type and different optimal type-specific thresholds could be defined.

For seizure-free (SF) patients the resection area is, by definition, a better representation of the epileptogenic zone than for non-seizure-free ones (NSF). Thus, one might expect that modelled epidemics spreading from the resection area might also reproduce the clinically observed seizure propagation patterns better for SF patients than for NSF ones. In order to test this hypothesis, we compared the correlations between the modelled and the clinical propagation patterns for SF and NSF patients. We found no significant differences for any of the cases considered (i.e. using either the resection area or the SEEG-based SOZ as seed). The limited spatio-temporal resolution of the clinical propagation profile might be partially accountable for this result. The small group size (10 patients, only 3 of whom were NSF) prevents any further interpretations of this result. It is still worth noting, however, that in the current setting all patients had a big improvement in the frequency and severity of the seizures [2, 59], so the resection area provided a reasonable approximation for the EZ, even for the NSF patients.

4.3 Modelling Resections

The effect of different resections on seizure propagation can be studied with the model by implementing virtual resections (see figure 5). One can then search for optimal resections that minimize seizure propagation for a given resection size. This can be used to aid epilepsy surgery by either finding resections that are smaller than the standard clinical approach, but have the same or almost the same effect [41], to find alternative resections that avoid specific regions [40], such as eloquent cortex, or to propose alternative resections, including regions outside the hypothesized SOZ, that might lead to a better outcome for NSF patients.

The problem of optimization of virtual resections is highly computationally demanding. We found that a method that combines topological – using a surrogate structural measure [57, 58] – and dynamical properties can find optimal resections on the network. The use of this surrogate measure allows for a fast exploration of the space of possible resections, which is followed by a slower analysis using the SI dynamics to fine-tune the solution and measure the actual decrease in seizure propagation. In future studies exact results of the SI propagation on a network could also be implemented to avoid the need for random search methods [82, 95], taking advantage of

549 the mathematical tractability of the SI model.

550 The effect of a resection in the model was measured as the decrease in propagation at a given time t_0 . That
551 is, we measured the slowing down of seizure propagation due to the resection. In the model, a complete stop
552 of propagation can only be achieved with – and is always achieved by – the complete disconnection of the seed
553 from the rest of the network (this may not imply complete seed removal, in some cases removal of the nodes
554 connecting the seed to the rest of the network might be enough and more efficient). This is because in the SI
555 model activity always spreads to every connected region, eventually, regardless of any other network or model
556 parameter. However, this model is only an approximation of actual seizure propagation, which is assumed to
557 hold only for small times in which seizure dynamics are dominated by the activity propagation processes. After
558 that, deactivation mechanisms kick in and the epileptiform activity eventually dies out. Within this paradigm,
559 a sufficient decrease in seizure propagation at a given (early) time t_0 would be enough to indicate an effective
560 resection (that is likely to lead to seizure freedom); here this threshold was set to 90% of the original infection
561 rate at time t_0 . Thus, we defined the optimal resection for each patient as the smallest resection leading to at
562 least 90% decrease in seizure propagation. We found in the model that this optimal resection was smaller than
563 the actual resection area for 7 out of 10 patients. Moreover, for four patients we found that it was possible to stop
564 seizure propagation at the fixed time t_0 with a resection smaller than the resection area. We found that cases
565 with a larger or more densely connected epileptogenic region (i.e. a larger seed for the SI dynamics) required a
566 larger portion of the seed to be removed to consistently reduce seizure propagation.

567 These findings highlight the need to devise patient-specific models to aid epilepsy surgery planning, so that
568 optimized individualized resections with minimal side-effects can be found. In this study we allowed the search
569 algorithm to consider nodes outside the resection area as targets for the virtual resections. We found that, for
570 one patient, the optimal 90% resection included one node outside the RA, and similarly for another patient the
571 100% resection also included one node outside the resection area. Thus, individualized models could in some
572 cases suggest alternative resections outside of the suspected epileptogenic zone that might be more beneficial
573 than standard surgery.

574 The 90% threshold for the reduction in seizure propagation was set ad-hoc and was equal for all patients, which
575 might not be realistic. Future studies could include a patient-specific estimation of the propagation threshold by
576 analyzing the individual intracranial EEG recordings: often epileptiform activity appears in a confined region
577 but does not propagate to the rest of the network. Information about the size of this region could be used to
578 estimate the threshold for which a reduction in seizure propagation in the model is considered sufficient, that
579 is, for which the modelled activity remains within this local region. Alternatively, de-activation mechanisms
580 could be introduced in the dynamical model, such as in the SIR model [41]. By setting the model initially
581 in the super-critical regime – in which seizures have a non-zero probability of propagating, the optimal resection
582 would be the one that takes the model to the subcritical regime with the minimum resection size. However, the
583 parameters of the model – namely the propagation and de-activation probabilities – would strongly affect this
584 result: if the system is initially far into the super-critical regime, a larger resection will be necessary compared to
585 when it is close to the critical transition. In fact, the SI model as it was used here corresponds to the highly-super
586 critical case in which seizures always spread. Thus, in order to avoid more assumptions that would hinder the
587 interpretation of the outcomes of such a model, the SIR parameters would need to be tuned with clinical data,
588 using for instance high-resolution spatio-temporal seizure-propagation patterns [36, 44, 96].

589 4.3.1 Alternative Resections for NSF patients

590 Another implication of the model definition is the fact that complete removal or isolation of the seed always leads
591 to complete stop of seizure propagation, because seizures, in the model, only generate within the seed. Within
592 the current formulation of the model, the seed is defined ad-hoc from the clinical data, either according to the
593 resection area (RA seed) or the pre-surgical clinical information (SOZ seed). This implies that the resection
594 model cannot distinguish situations where the selected seed is not a good representation of the EZ, such as is
595 the case for NSF patients, and suggest a better resection. The first part of the model, i.e. the reproduction of
596 seizure propagation patterns, could be of aid: the plausibility of different seeds can be judged from the maximum
597 correlation that they yield between the modelled seizure patterns and the clinical SEEG patterns. Thus, optimal
598 seed definitions that maximally reproduce the observed seizure propagation patterns could be suggested. This
599 hypothesis implies that a higher correlation should be found for SF than for NSF patients when considering
600 the resection area as the seed, which we were not able to validate in this study due to the small group size.
601 Future studies should tackle this issue with larger patient groups and possibly more detailed spatio-temporal
602 seizure propagation patterns, to increase the model resolution. Moreover, this would also validate whether the
603 model can provide independent information prospectively – that is, prior to surgery – and suggest optimal seed
604 definitions.

4.4 Strengths

The main strength of our approach is the simplicity of the model considered. Epidemic spreading models do not intent to capture the details of the underlying biological basis of seizure generation and propagation, only the stereotypical patterns of seizure propagation [85]. The simplicity of the model not only allows for faster calculations and fewer free parameters, but it also comes with a large body of theoretical and computational studies that can be used to interpret the results and design the study [51].

We integrated data from different modalities that are commonly measured in clinical practice: MEG and SEEG recordings, and the location of the resection area. The use of MEG networks as a proxy for structural networks avoids the computation of structural DTI networks, which are not part of standard clinical care and also time-consuming, limiting the flexibility with which the choice of atlas can be changed. Using AEC-MEG networks to define the backbone for the dynamical model allows for more versatility, as well as the ability to use our approach in patients for whom DTI data are not available, [reducing the burden associated with the use of computational models in clinical practice](#).

The model was fitted with patient-specific data and optimized independently for each patient. The varying results for different patients, both for the reproduction of seizure propagation patterns and the analysis of alternative resections, highlight the need for using personalized models of seizure propagation [36, 41, 96].

Moreover, the model could be easily extended to include more clinical presurgical information, such as the existence of MRI or MEG abnormalities. Similarly, the model could be used prospectively by using alternative definitions of the seed, that do not depend on the resection area, as we have already shown here by using seeds based on the SOZ as determined from SEEG (see figures 6 and 7).

4.5 Limitations

The main limitations of the current study are the limited number of patients considered and the low-resolution of the clinical seizure propagation patterns. The small cohort prevents further validation of the model to distinguish between SF and NSF patients. Meanwhile, the low resolution implies that few parameters of the dynamical model can be fit to the data. [Future studies should consider larger patient cohorts in order to validate the model performance. In this study a small cohort was used as proof-of-concept, since both the manual processing of the data and the computational analyses are highly temporally expensive.](#)

Another important limitation is that the seed of seizure propagation was assumed from the data – being either the resection area or the SOZ as estimated from the SEEG recordings. This, in conjunction with the fact that complete removal of the seed always leads to a stop of seizure propagation, implies that the model cannot suggest better resections for NSF patients, and it also limits its prospective use. To be of more clinical use, the model should be able to suggest the seed of seizure propagation. This could be done by finding the set of nodes that maximally reproduces the clinical seizure propagation patterns. However, in order to do this realistically and in a systematic manner, more detailed spatio-temporal patterns of seizure propagation are needed for each patient. These could be obtained from the SEEG recordings directly [36, 44, 96].

Another limitation is the nature of the SI model: it reproduces adequately the initial steps of seizure propagation, but the lack of a de-activation mechanism means that it cannot fit the whole seizure. Including a mechanism for de-activation would circumvent this issue, provided that the extra parameters can be adequately fitted. [Similarly, in this study we have used MEG-AEC networks as surrogate for structural connectivity, instead of actual structural networks as those derived with DTI.](#)

The use of SEEG data to fit the model can be another limitation for its clinical use, as SEEG recordings are highly invasive and not always part of the presurgical evaluation. However, we have shown that the model parameters can be extrapolated from the overall best fit (see figure 6c) and used for patients without SEEG. In the current setting, this led to a less than 15% decrease in the reproducibility of the seizure patterns, as measured by the correlation between the SI and SEEG propagation patterns. Information from other modalities could also potentially be included, such as epileptiform abnormalities found in MEG imaging. These can be used to set the probability for a region being a seed region.

An inherent limitation of all studies analyzing the functional effect of different resections is modeling the resection itself. Here we have employed the commonly used *virtual resection* technique, such that the weights of all resected links are set to 0 [37, 86, 97, 98]. This does not account for the generalized effect that a local resection can have on the network [99]. It does not consider any plasticity mechanisms either [100, 101], which are known to occur following a lesion in the brain [11, 102] – and in particular following a resection [81, 103–105]. These appear as a consequence of the network disruption, and can have widespread effects. They will play a significant role in the cognitive functioning following the resection, and can also affect the long-term outcome of the surgery. These effects should be included in future studies for a more comprehensive modelling of epilepsy

660 surgery.

661 In this study we decided to identify the resection areas by applying an affine transformation of the post-
662 surgical MRI to the pre-surgical MRI, as it is common practice in computational studies of epilepsy surgery
663 [27, 30, 35, 36, 41, 44, 81]. Recent studies using multi-modal imaging or intra-surgical imaging have found a
664 better characterization of resection areas using more general transformations such as elastic models [106–108].
665 Potential differences arise in particular for large resections, but are unlikely to be significant at an atlas-level
666 resolution, and visual inspection in our data-set identified only small variations at the sub-ROI level. Future
667 studies should approach this perspective and characterize the actual significance of brain tissue adaptation after
668 the surgery and the convenience of considering elastic coregistrations to characterize the resection cavities.

669 A final limitation of the study, and of similar studies using the virtual resection technique, is the difficulty
670 of the validation of the results, as the different resections cannot be tested clinically. Typically, virtual resection
671 models are validated by comparing the overlap between the suspected EZ as generated by the model with the
672 resection area for both SF and NSF patients, where a valid model should provide a good match for SF patients
673 and a poor match for NSF patients [32, 35, 37, 38, 42]. Alternatively, the propagation pathways simulated by
674 the model are compared with those recorded with SEEG [36, 96]. We have undertaken the later approach in this
675 work to tune the model parameters and for validation, and the first approach was used for validation, although
676 the small group sizes do not allow us to draw strong conclusions in this proof-of-principle study. Moreover, using
677 surgical outcome to validate the model is only a first step, as the ultimate goal is to improve surgical outcome,
678 i.e. to perform the analysis proposed in this work before surgery has taken place.

679 4.6 Outlook

680 In recent years there have been increasing efforts to develop individualized computer models to study brain
681 disorders. In particular, in the case of epilepsy surgery, it is expected that such models might help improve
682 surgery outcome and decrease the cognitive side-effects associated with epilepsy surgery, by proposing targeted,
683 individualized resections for each patient. Currently, the greatest challenge remains in the validation of the
684 models, as the ground truth is inherently missing and the actual effect of a resection can only be known several
685 months – or years – after the surgery has taken place. Thus, extensive retrospective validation of the models is
686 necessary before prospective (or even pseudo-prospective) studies can take place. Here, the seizure propagation
687 model ought to be validated in future studies by increasing the number of included patients, and the resolution
688 of the SEEG seizure propagation pattern should be increased in order to increase the sensitivity to the model
689 parameters. Then, if a better relation between the model and the clinical data can be found for SF than for NSF
690 patients, as we have hypothesized, the model could be used to find the seed regions that maximally reproduce
691 the seizure patterns. Similarly, future studies could explicitly include forbidden areas that cannot be removed
692 during the surgery, such as the eloquent cortex, or avoid surgeries that are not possible in clinical practice.

693 5 Conclusions

694 Patient-specific epidemic models can capture the fundamental aspects of seizure propagation as observed clini-
695 cally with invasive SEEG recordings. The models, optimized specifically for each patient, can then be used to test
696 the effect that different resection strategies may have on seizure propagation *in silico*. Our results highlight the
697 need for individualized computer models to aid epilepsy surgery planning by defining smaller targeted resections
698 with potentially fewer side-effects and better outcome than standard surgery.

699 6 Acknowledgements

700 Ana P. Millán and Ida A. Nissen were supported by ZonMw and the Dutch Epilepsy Foundation, project number
701 95105006. The funding sources had no role in study design, data collection and analysis, interpretation of results,
702 decision to publish, or preparation of the manuscript.

703 7 Competing Interests

704 The authors declare that they have no competing interests.

8 Author Contributions

A.P.M., E.C.W.S., C.J.S., I.A.N, A.H. conceptualized the study, E.C.W.S., C.J.S., I.A.N, S.I., J.C.B., P.V.M., A.H. participated in the funding acquisition, A.P.M, E.C.W.S., C.J.S, A.H. devised the Methodology, A.P.M. performed the formal analysis, A.P.M, I.A.N, A.H. devised the software and visualization E.C.W.S., C.J.S., P.V.M., A.H. participated in the supervision, E.C.W.S., S.I., J.C.B. provided resources, A.P.M. wrote the original draft and all authors participated in writing review and editing.

References

- [1] P. N. Banerjee, D. Filippi, and W. A. Hauser. “The descriptive epidemiology of epilepsy—a review”. *Epilepsy Research* 85.1 (2009).
- [2] A. T. Berg et al. “Revised terminology and concepts for organization of seizures and epilepsies: report of the ILAE Commission on Classification and Terminology, 2005–2009”. *Epilepsia* 51.4 (2010).
- [3] O. C. González et al. “Ionic and synaptic mechanisms of seizure generation and epileptogenesis”. *Neurobiology of Disease* 130 (2019).
- [4] K. Lehnertz et al. “Synchronization phenomena in human epileptic brain networks”. *Journal of Neuroscience Methods* 183.1 (2009).
- [5] F. L. Da Silva et al. “Epilepsies as dynamical diseases of brain systems: basic models of the transition between normal and epileptic activity”. *Epilepsia* 44 (2003).
- [6] P. Kwan et al. “Definition of drug resistant epilepsy: consensus proposal by the ad hoc Task Force of the ILAE Commission on Therapeutic Strategies”. *Epilepsia* 51.6 (2010).
- [7] D. J. Englot et al. “Epileptogenic zone localization using magnetoencephalography predicts seizure freedom in epilepsy surgery”. *Epilepsia* 56.6 (2015).
- [8] B. C. Jobst and G. D. Cascino. “Resective epilepsy surgery for drug-resistant focal epilepsy: a review”. *Jama* 313.3 (2015).
- [9] H. O. Lüders et al. “The epileptogenic zone: general principles”. *Epileptic Disorders* 8.2 (2006).
- [10] M. A. Kramer and S. S. Cash. “Epilepsy as a disorder of cortical network organization”. *The Neuroscientist* 18.4 (2012).
- [11] C. J. Stam. “Modern network science of neurological disorders”. *Nature Reviews Neuroscience* 15.10 (2014).
- [12] E. H. Smith and C. A. Schevon. “Toward a mechanistic understanding of epileptic networks”. *Current neurology and neuroscience reports* 16.11 (2016).
- [13] L. Douw et al. “Epilepsy is related to theta band brain connectivity and network topology in brain tumor patients”. *BMC Neuroscience* 11.1 (2010).
- [14] M. Pedersen et al. “Increased segregation of brain networks in focal epilepsy: an fMRI graph theory finding”. *NeuroImage: Clinical* 8 (2015).
- [15] G. Bettus et al. “Decreased basal fMRI functional connectivity in epileptogenic networks and contralateral compensatory mechanisms”. *Human Brain Mapping* 30.5 (2009).
- [16] Z. Zhang et al. “Altered functional–structural coupling of large-scale brain networks in idiopathic generalized epilepsy”. *Brain* 134.10 (2011).
- [17] M. Centeno and D. W. Carmichael. “Network connectivity in epilepsy: resting state fMRI and EEG–fMRI contributions”. *Frontiers in Neurology* 5 (2014).
- [18] G. J. Ortega et al. “Impaired mesial synchronization in temporal lobe epilepsy”. *Clinical Neurophysiology* 122.6 (2011).
- [19] G. Bettus et al. “Interictal functional connectivity of human epileptic networks assessed by intracerebral EEG and BOLD signal fluctuations”. *PLoS ONE* 6.5 (2011).

- 750 [20] F. Pittau et al. “Patterns of altered functional connectivity in mesial temporal lobe epilepsy”.
751 *Epilepsia* 53.6 (2012).
- 752 [21] M. P. van den Heuvel and O. Sporns. “Network hubs in the human brain”. *Trends in cognitive*
753 *sciences* 17.12 (2013).
- 754 [22] N. A. Crossley et al. “The hubs of the human connectome are generally implicated in the anatomy
755 of brain disorders”. *Brain* 137.8 (2014).
- 756 [23] R. J. Morgan and I. Soltesz. “Nonrandom connectivity of the epileptic dentate gyrus predicts
757 a major role for neuronal hubs in seizures”. *Proceedings of the National Academy of Sciences*
758 105.16 (2008).
- 759 [24] B. C. Bernhardt et al. “Graph-theoretical analysis reveals disrupted small-world organization of
760 cortical thickness correlation networks in temporal lobe epilepsy”. *Cerebral Cortex* 21.9 (2011).
- 761 [25] S.-H. Jin, W. Jeong, and C. K. Chung. “Mesial temporal lobe epilepsy with hippocampal sclerosis
762 is a network disorder with altered cortical hubs”. *Epilepsia* 56.5 (2015).
- 763 [26] W. Liao et al. “Altered functional connectivity and small-world in mesial temporal lobe epilepsy”.
764 *PLoS ONE* 5.1 (2010).
- 765 [27] I. A. Nissen et al. “Identifying the epileptogenic zone in interictal resting-state MEG source-space
766 networks”. *Epilepsia* 58.1 (2017).
- 767 [28] S. Tavakol et al. “Neuroimaging and connectomics of drug-resistant epilepsy at multiple scales:
768 From focal lesions to macroscale networks”. *Epilepsia* 60.4 (2019).
- 769 [29] I. Najm et al. “Temporal patterns and mechanisms of epilepsy surgery failure”. *Epilepsia* 54.5
770 (2013).
- 771 [30] I. A. Nissen et al. “Localization of the epileptogenic zone using interictal MEG and machine
772 learning in a large cohort of drug-resistant epilepsy patients”. *Frontiers in Neurology* 9 (2018).
- 773 [31] J. Hebbink et al. “Phenomenological network models: Lessons for epilepsy surgery”. *Epilepsia*
774 58.10 (2017).
- 775 [32] M. A. Lopes et al. “An optimal strategy for epilepsy surgery: Disruption of the rich-club?” *PLoS*
776 *Computational Biology* 13.8 (2017).
- 777 [33] F. Hutchings et al. “Predicting surgery targets in temporal lobe epilepsy through structural
778 connectome based simulations”. *PLoS Computational Biology* 11.12 (2015).
- 779 [34] C. Yang et al. “Localization of epileptogenic zone with the correction of pathological networks”.
780 *Frontiers in Neurology* 9 (2018).
- 781 [35] M. Goodfellow et al. “Estimation of brain network ictogenicity predicts outcome from epilepsy
782 surgery”. *Scientific Reports* 6.1 (2016). Number: 1 Publisher: Nature Publishing Group.
- 783 [36] T. Proix et al. “Individual brain structure and modelling predict seizure propagation”. *Brain*
784 140.3 (2017). Publisher: Oxford Academic.
- 785 [37] N. Sinha et al. “Predicting neurosurgical outcomes in focal epilepsy patients using computational
786 modelling”. *Brain* 140.2 (2017). Publisher: Oxford Academic.
- 787 [38] A. Steimer, M. Müller, and K. Schindler. “Predictive modeling of EEG time series for evaluating
788 surgery targets in epilepsy patients”. *Human Brain Mapping* 38.5 (2017).
- 789 [39] P. N. Taylor, M. Kaiser, and J. Dauwels. “Structural connectivity based whole brain modelling
790 in epilepsy”. *Journal of Neuroscience Methods* 236 (2014).
- 791 [40] S. An et al. “Optimization of surgical intervention outside the epileptogenic zone in the Virtual
792 Epileptic Patient (VEP)”. *PLoS Computational Biology* 15.6 (2019).
- 793 [41] I. A. Nissen et al. “Optimization of epilepsy surgery through virtual resections on individual
794 structural brain networks”. *Scientific reports* 11.1 (2021).

- 795 [42] M. A. Lopes et al. “Elevated ictal brain network ictogenicity enables prediction of optimal seizure
796 control”. *Frontiers in Neurology* 9 (2018).
- 797 [43] P. Laiou et al. “Quantification and selection of ictogenic zones in epilepsy surgery”. *Frontiers in*
798 *Neurology* 10 (2019).
- 799 [44] V. Sip et al. “Data-driven method to infer the seizure propagation patterns in an epileptic brain
800 from intracranial electroencephalography”. *PLoS Computational Biology* 17.2 (2021).
- 801 [45] M. A. Lopes et al. “Computational modelling in source space from scalp EEG to inform presur-
802 gical evaluation of epilepsy”. *Clinical Neurophysiology* 131.1 (2020).
- 803 [46] M. J. Koeppe and F. G. Woermann. “Imaging structure and function in refractory focal epilepsy”.
804 *The Lancet Neurology* 4.1 (2005).
- 805 [47] G. L. Barkley. “Controversies in neurophysiology. MEG is superior to EEG in localization of
806 interictal epileptiform activity: Pro”. *Clinical Neurophysiology* 115.5 (2004).
- 807 [48] J. S. Ebersole and S. M. Ebersole. “Combining MEG and EEG source modeling in epilepsy
808 evaluations”. *Journal of Clinical Neurophysiology* 27.6 (2010).
- 809 [49] L. Junges et al. “The role that choice of model plays in predictions for epilepsy surgery”. *Scientific*
810 *Reports* 9.1 (2019).
- 811 [50] A. Barrat, M. Barthelemy, and A. Vespignani. *Dynamical processes on complex networks*. Cam-
812 bridge University Press, 2008.
- 813 [51] R. Pastor-Satorras et al. “Epidemic processes in complex networks”. *Reviews of Modern Physics*
814 87.3 (2015).
- 815 [52] L. R. Peraza et al. “Structural connectivity centrality changes mark the path toward Alzheimer’s
816 disease”. *Alzheimer’s & Dementia: Diagnosis, Assessment & Disease Monitoring* 11 (2019).
- 817 [53] C. J. Stam et al. “The relation between structural and functional connectivity patterns in complex
818 brain networks”. *International Journal of Psychophysiology*. Research on Brain Oscillations and
819 Connectivity in A New Take-Off State 103 (2016).
- 820 [54] J. O. Lloyd-Smith et al. “Superspreading and the effect of individual variation on disease emer-
821 gence”. *Nature* 438.7066 (2005).
- 822 [55] R. Pastor-Satorras and A. Vespignani. “Immunization of complex networks”. *Physical review E*
823 65.3 (2002).
- 824 [56] Z. Dezső and A.-L. Barabási. “Halting viruses in scale-free networks”. *Physical Review E* 65.5
825 (2002).
- 826 [57] D. Brockmann and D. Helbing. “The hidden geometry of complex, network-driven contagion
827 phenomena”. *Science* 342.6164 (2013).
- 828 [58] P. C. Pinto, P. Thiran, and M. Vetterli. “Locating the source of diffusion in large-scale networks”.
829 *Physical review Letters* 109.6 (2012).
- 830 [59] J. Engel Jr. “Outcome with respect to epileptic seizures.” *Surgical treatment of the epilepsies*
831 (1993).
- 832 [60] M. Ercsey-Ravasz et al. “A predictive network model of cerebral cortical connectivity based on
833 a distance rule”. *Neuron* 80.1 (2013).
- 834 [61] R. Gămănuț et al. “The mouse cortical connectome, characterized by an ultra-dense cortical
835 graph, maintains specificity by distinct connectivity profiles”. *Neuron* 97.3 (2018).
- 836 [62] P. Theodoni et al. “Structural attributes and principles of the neocortical connectome in the
837 marmoset monkey”. *BioRxiv* (2020).
- 838 [63] J. A. Roberts et al. “Consistency-based thresholding of the human connectome”. *NeuroImage*
839 145 (2017).

- 840 [64] G. Deco and M. L. Kringelbach. “Turbulent-like dynamics in the human brain”. *Cell reports*
841 33.10 (2020).
- 842 [65] G. Deco et al. “Rare long-range cortical connections enhance human information processing”.
843 *Current Biology* 31.20 (2021).
- 844 [66] A. Hillebrand et al. “Feasibility of clinical magnetoencephalography (MEG) functional mapping
845 in the presence of dental artefacts”. *Clinical Neurophysiology* 124.1 (2013).
- 846 [67] S. Taulu and J. Simola. “Spatiotemporal signal space separation method for rejecting nearby
847 interference in MEG measurements”. *Physics in Medicine & Biology* 51.7 (2006).
- 848 [68] S. Taulu and R. Hari. “Removal of magnetoencephalographic artifacts with temporal signal-space
849 separation: demonstration with single-trial auditory-evoked responses”. *Human Brain Mapping*
850 30.5 (2009).
- 851 [69] A. Hillebrand et al. “Frequency-dependent functional connectivity within resting-state networks:
852 an atlas-based MEG beamformer solution”. *Neuroimage* 59.4 (2012).
- 853 [70] A. Hillebrand et al. “Direction of information flow in large-scale resting-state networks is frequency-
854 dependent”. *Proceedings of the National Academy of Sciences* 113.14 (2016).
- 855 [71] L. Fan et al. “The human brainnetome atlas: a new brain atlas based on connectional architec-
856 ture”. *Cerebral Cortex* 26.8 (2016).
- 857 [72] K. Sekihara et al. “Asymptotic SNR of scalar and vector minimum-variance beamformers for neu-
858 romagnetic source reconstruction”. *IEEE Transactions on Biomedical Engineering* 51.10 (2004).
- 859 [73] D. Cheyne et al. “Event-related beamforming: a robust method for presurgical functional mapping
860 using MEG”. *Clinical Neurophysiology* 118.8 (2007).
- 861 [74] M. Xia, J. Wang, and Y. He. “BrainNet Viewer: a network visualization tool for human brain
862 connectomics”. *PLoS ONE* 8.7 (2013).
- 863 [75] *Brainwave*. <https://home.kpn.nl/stam7883/brainwave.html>.
- 864 [76] A. Bruns et al. “Amplitude envelope correlation detects coupling among incoherent brain signals”.
865 *Neuroreport* 11.7 (2000).
- 866 [77] M. J. Brookes et al. “Measuring functional connectivity using MEG: methodology and comparison
867 with fcMRI”. *Neuroimage* 56.3 (2011).
- 868 [78] J. F. Hipp et al. “Large-scale cortical correlation structure of spontaneous oscillatory activity”.
869 *Nature Neuroscience* 15.6 (2012).
- 870 [79] G. L. Colclough et al. “How reliable are MEG resting-state connectivity metrics?” *Neuroimage*
871 138 (2016).
- 872 [80] C. T. Briels et al. “In pursuit of a sensitive EEG functional connectivity outcome measure for
873 clinical trials in Alzheimer’s disease”. *Clinical Neurophysiology* 131.1 (2020).
- 874 [81] M. K. Sidhu et al. “Memory network plasticity after temporal lobe resection: a longitudinal
875 functional imaging study”. *Brain* 139.2 (2016).
- 876 [82] P. Van Mieghem and K. Devriendt. “An epidemic perspective on the cut size in networks”. *Delft*
877 *University of Technology, Report* 20180312 (2018).
- 878 [83] P. Van Mieghem. “Universality of the SIS prevalence in networks”. *arXiv preprint arXiv:1612.01386*
879 (2016).
- 880 [84] S. Kirkpatrick, C. D. Gelatt, and M. P. Vecchi. “Optimization by simulated annealing”. *Science*
881 220.4598 (1983).
- 882 [85] F. Wendling et al. “Computational models of epileptiform activity”. *Journal of Neuroscience*
883 *Methods* 260 (2016).
- 884 [86] L. G. Kini et al. “Virtual resection predicts surgical outcome for drug-resistant epilepsy”. *Brain*
885 142.12 (2019).

- 886 [87] M. Hashemi et al. “The Bayesian Virtual Epileptic Patient: A probabilistic framework designed
887 to infer the spatial map of epileptogenicity in a personalized large-scale brain model of epilepsy
888 spread”. *NeuroImage* (2020).
- 889 [88] J. Courtiol et al. “Dynamical Mechanisms of Interictal Resting-State Functional Connectivity
890 in Epilepsy”. *Journal of Neuroscience* 40.29 (2020). Publisher: Society for Neuroscience Section:
891 Research Articles.
- 892 [89] E. Cator and P. Van Mieghem. “Susceptible-infected-susceptible epidemics on the complete graph
893 and the star graph: Exact analysis”. *Physical Review E* 87.1 (2013).
- 894 [90] U. T. Srinivasan et al. “Response of complex food webs to realistic extinction sequences”. *Ecology*
895 88.3 (2007).
- 896 [91] J. P. Gleeson. “Cascades on correlated and modular random networks”. *Physical Review E* 77.4
897 (2008).
- 898 [92] N. Masuda and P. Holme. “Predicting and controlling infectious disease epidemics using temporal
899 networks”. *F1000prime reports* 5 (2013).
- 900 [93] O. E. Williams et al. “The shape of memory in temporal networks”. *arXiv preprint arXiv:2004.12784*
901 (2020).
- 902 [94] P. Van Mieghem et al. “Influence of assortativity and degree-preserving rewiring on the spectra
903 of networks”. *The European Physical Journal B* 76.4 (2010).
- 904 [95] B. Prasse and P. Van Mieghem. “Time-dependent solution of the NIMFA equations around the
905 epidemic threshold”. *Journal of Mathematical Biology* 81.6 (2020).
- 906 [96] S. Olmi et al. “Controlling seizure propagation in large-scale brain networks”. *PLoS Computa-*
907 *tional Biology* 15.2 (2019).
- 908 [97] B. E. Youngerman and G. M. McKhann. “From Nodes to Networks: Can Virtual Resections
909 Predict Neurosurgical Outcomes in Focal Epilepsy?” *Neurosurgery* 81.3 (2017). Publisher: Oxford
910 Academic.
- 911 [98] V. K. Jirsa et al. “The virtual epileptic patient: individualized whole-brain models of epilepsy
912 spread”. *Neuroimage* 145 (2017).
- 913 [99] M. Demuru et al. “Validation of virtual resection on intraoperative interictal data acquired during
914 epilepsy surgery”. *Journal of Neural Engineering* 17.6 (2020).
- 915 [100] A. Holtmaat and K. Svoboda. “Experience-dependent structural synaptic plasticity in the mam-
916 malian brain”. *Nature Reviews Neuroscience* 10.9 (2009).
- 917 [101] A. P. Millán et al. “Concurrence of form and function in developing networks and its role in
918 synaptic pruning”. *Nature Communications* 9.1 (2018).
- 919 [102] C. J. Stam et al. “Emergence of modular structure in a large-scale brain network with interactions
920 between dynamics and connectivity”. *Frontiers in Computational Neuroscience* 4 (2010).
- 921 [103] Y. Tao and B. Rapp. “Investigating the network consequences of focal brain lesions through
922 comparisons of real and simulated lesions”. *Scientific Reports* 11.1 (2021).
- 923 [104] M. Yogarajah et al. “The structural plasticity of white matter networks following anterior tem-
924 poral lobe resection”. *Brain* 133.8 (2010).
- 925 [105] J. Stretton et al. “Working memory network plasticity after anterior temporal lobe resection: a
926 longitudinal functional magnetic resonance imaging study”. *Brain* 137.5 (2014).
- 927 [106] M. Riva et al. “Intraoperative computed tomography and finite element modelling for multimodal
928 image fusion in brain surgery”. *Operative Neurosurgery* 18.5 (2020).
- 929 [107] S. Senova et al. “Case Report: Multimodal Functional and Structural Evaluation Combining
930 Pre-operative nTMS Mapping and Neuroimaging With Intraoperative CT-Scan and Brain Shift
931 Correction for Brain Tumor Surgical Resection”. *Frontiers in human neuroscience* 15 (2021).

- 932 [108] F. Pérez-Garcia et al. “Simulation of brain resection for cavity segmentation using self-supervised
933 and semi-supervised learning”. *International Conference on Medical Image Computing and Computer-*
934 *Assisted Intervention*. Springer. 2020.